PLOS COMPUTATIONAL BIOLOGY

RESEARCH ARTICLE

Regulation of adenylyl cyclase 5 in striatal neurons confers the ability to detect coincident neuromodulatory signals

Neil J. Bruce[1☯], Daniele Narzi[2☯], Daniel Trpevski[3☯], Siri C. van Keulen[2,4☯], Anu G. Nair[5], Ursula Röthlisberger[2]*, Rebecca C. Wade[1,6,7]*, Paolo Carloni[8,9,10,11]*, Jeanette Hellgren Kotaleski[3,12]*

1 Molecular and Cellular Modeling Group, Heidelberg Institute for Theoretical Studies (HITS), Schloss-Heidelberg, Germany, **2** Institut des Sciences et Ingénierie Chimiques, École Polytechnique Fédérale de Lausanne (EPFL), CH-1015 Lausanne, Switzerland, **3** Science for Life Laboratory, School of Electrical Engineering and Computer Science, KTH Royal Institute of Technology, Stockholm, Sweden, **4** Department of Computer Science, Stanford University, Stanford, California, United States of America, **5** Institute of Molecular Life Sciences, University of Zurich, Zurich, Switzerland, **6** Center for Molecular Biology (ZMBH), DKFZ-ZMBH Alliance, Heidelberg University, Heidelberg, Germany, **7** Interdisciplinary Center for Scientific Computing (IWR), Heidelberg University, Heidelberg, Germany, **8** Department of Physics and Department of Neurobiology, RWTH Aachen University,Aachen, Germany, **9** Institute for Neuroscience and Medicine (INM)-11, Forschungszentrum Jülich, Jülich, Germany, **10** Institute of Neuroscience and Medicine (INM-9), Forschungszentrum Jülich, Jülich, Germany, **11** Institute for Advanced Simulation (IAS-5), Forschungszentrum Jülich, Jülich, Germany, **12** Department of Neuroscience, Karolinska Institutet, Solna, Sweden

☯ These authors contributed equally to this work.
* ursula.roethlisberger@epfl.ch (UR); rebecca.wade@h-its.org (RCW); p.carloni@fz-juelich.de (PC); jeanette@csc.kth.se (JHK)

Citation: Bruce NJ, Narzi D, Trpevski D, van Keulen SC, Nair AG, Röthlisberger U, et al. (2019) Regulation of adenylyl cyclase 5 in striatal neurons confers the ability to detect coincident neuromodulatory signals. PLoS Comput Biol 15 (10): e1007382. https://doi.org/10.1371/journal.pcbi.1007382

Editor: Hugues Berry, Inria, FRANCE

Received: April 1, 2019

Accepted: September 5, 2019

Published: October 30, 2019

Data Availability Statement: The data and models generated in this work are available for download and visualisation at https://humanbrainproject.github.io/hbp-bsp-live-papers/2019/bruce_et_al_2019/bruce_et_al_2019.html.

Funding: This research has received funding from the European Union Seventh Framework Programme (FP7/2007-2013; https://ec.europa.eu/research/fp7) under grant agreement N° 604102 (HBP) (JHK, PC, RCW), the European Union's Horizon 2020 Framework Programme (https://ec.

Abstract

Long-term potentiation and depression of synaptic activity in response to stimuli is a key factor in reinforcement learning. Strengthening of the corticostriatal synapses depends on the second messenger cAMP, whose synthesis is catalysed by the enzyme adenylyl cyclase 5 (AC5), which is itself regulated by the stimulatory $G\alpha_{olf}$ and inhibitory $G\alpha_i$ proteins. AC isoforms have been suggested to act as coincidence detectors, promoting cellular responses only when convergent regulatory signals occur close in time. However, the mechanism for this is currently unclear, and seems to lie in their diverse regulation patterns. Despite attempts to isolate the ternary complex, it is not known if $G\alpha_{olf}$ and $G\alpha_i$ can bind to AC5 simultaneously, nor what activity the complex would have. Using protein structure-based molecular dynamics simulations, we show that this complex is stable and inactive. These simulations, along with Brownian dynamics simulations to estimate protein association rates constants, constrain a kinetic model that shows that the presence of this ternary inactive complex is crucial for AC5's ability to detect coincident signals, producing a synergistic increase in cAMP. These results reveal some of the prerequisites for corticostriatal synaptic plasticity, and explain recent experimental data on cAMP concentrations following receptor activation. Moreover, they provide insights into the regulatory mechanisms that control signal processing by different AC isoforms.

europa.eu/programmes/horizon2020/en) for Research and Innovation under the Specific Grant Agreement N°s 720270 (Human Brain Project SGA1) (JHK, PC, RCW, UR, AGN) and 785907 (Human Brain Project SGA2) (JHK, PC, RCW, UR, DT), the Swedish e-Science Research Centre (SeRC; https://e-science.se/) (JHK, DT), the Swedish Research Council (https://www.vr.se/) (JHK, AGN, DT), the Klaus Tschira Stiftung (www.klaus-tschira-stiftung.de) (RCW, NJB), National Institute on Alcohol Abuse and Alcoholism Grant 2R01AA016022 (www.niaaa.nih.gov) (JHK). The funders had no role in study design, data collection and analysis, decision to publish, or preparation of the manuscript.

Competing interests: The authors have declared that no competing interests exist.

Author summary

Adenylyl cyclases (ACs) are enzymes that can translate extracellular signals into the intracellular molecule cAMP, which is thus a 2nd messenger of extracellular events. The brain expresses nine membrane-bound AC variants, and AC5 is the dominant form in the striatum. The striatum is the input stage of the basal ganglia, a brain structure involved in reward learning, i.e. the learning of behaviors that lead to rewarding stimuli (such as food, water, sugar, etc). During reward learning, cAMP production is crucial for strengthening the synapses from cortical neurons onto the striatal principal neurons, and its formation is dependent on several neuromodulatory systems such as dopamine and acetylcholine. It is, however, not understood how AC5 is activated by transient (subsecond) changes in the neuromodulatory signals. Here we combine several computational tools, from molecular dynamics and Brownian dynamics simulations to bioinformatics approaches, to inform and constrain a kinetic model of the AC5-dependent signaling system. We use this model to show how the specific molecular properties of AC5 can detect particular combinations of co-occuring transient changes in the neuromodulatory signals which thus result in a supralinear/synergistic cAMP production. Our results also provide insights into the computational capabilities of the different AC isoforms.

Introduction

Information processing in the brain occurs within circuits of neurons that are interconnected via synapses. The modification of these neuronal circuits, in response to an organism's experiences and interactions with the environment, is crucial for memory and learning, allowing the organism's behaviour to adapt to changing conditions in its environment. One way that neuronal circuits are modified is through the process of synaptic plasticity, in which the strengths of certain synapses are either enhanced or depressed over time in response to neural activity. Insights into when plasticity happens can provide an understanding of the basic functioning of the nervous system, and its ability to learn. A very informative way to gain such insights is through analyzing the molecular circuitry of the synapses - i.e. the networks of biochemical reactions that underlie synaptic modifications. These differ across synapses, and our focus in this study is on the corticostriatal synapse, which is the interface between the cortex and the basal ganglia, a forebrain structure involved in selection of behaviour and reward learning [1,2].

All cells process information from their external and internal environment through signal transduction networks - molecular circuits evolved for producing suitable responses to different stimuli. In neurons, synaptic signal transduction networks determine whether a synapse will be potentiated or depressed. In some cases, even single molecules are able to realize computational abilities within these networks. These molecules are often enzymes, whose activity is allosterically regulated by the binding of other signaling molecules [3]. One such case is the family of mammalian adenylyl cyclase enzymes (ACs). These catalyze the conversion of adenosine triphosphate (ATP) to cyclic adenosine monophosphate (cAMP) - one of the main cellular second messenger signaling molecules.

Mammalian ACs express ten different isoforms [4–6]. Of these, nine are membrane bound, and one is soluble. Their catalytic reaction may be regulated by a variety of interactors, most importantly G protein subunits [6]. These are released in response to extracellular agonists binding to G protein-coupled receptors (GPCRs), the largest superfamily of mammalian

transmembrane receptors. In this way, ACs may function not only as signal transducers but also as *signal integrators*: they perform decision functions that determine the time at which and how much cAMP is produced. One such decision function, attributed to many ACs, is detection of co-occuring signaling events (denoted as *coincidence detection* here), resulting in significantly increased production of cAMP only when more than one signaling event occurs almost simultaneously [7–15].

All nine membrane-bound AC isoforms are expressed in the brain, possibly because this organ is specialized in signal processing. Specific ACs are particularly abundant in specific brain regions, and AC5 is highly expressed in the striatum, the input nucleus of the basal ganglia. It is involved in signal transduction networks that are crucial for synaptic plasticity in the two types of medium spiny neurons (MSNs) of this brain region, which are the direct pathway MSNs that express D_1-type dopamine receptors (D_1 MSNs), and the indirect pathway MSNs expressing D_2-type dopamine receptors (D_2 MSNs).

The same regulatory mechanism exists in both MSN types: AC5 is activated by the stimulatory $G\alpha_{olf}$ protein subunit, and inhibited by the inhibitory $G\alpha_i$ protein subunit. Clearly, the regulation of AC5 is a crucial determinant of the levels of cAMP. This mechanism responds to different extracellular agonists (acting as neuromodulatory signals) associated with the expression of different G protein-coupled receptors (GPCRs) (Fig 1A) [16–18]. In D_1 MSNs, the binding of dopamine to the D_1 GPCR results in the release of $G\alpha_{olf}$, while binding of acetylcholine to the M_4 GPCR causes the release of $G\alpha_i$. Conversely, in D_2 MSNs, binding of dopamine to the D_2 GPCRs results in the release of $G\alpha_i$, and $G\alpha_{olf}$ is released upon binding of adenosine to the A_{2a} GPCR.

Knowing how AC5 processes the neuromodulatory signals would reveal the conditions under which plasticity and learning in the basal ganglia are triggered. In particular, knowing

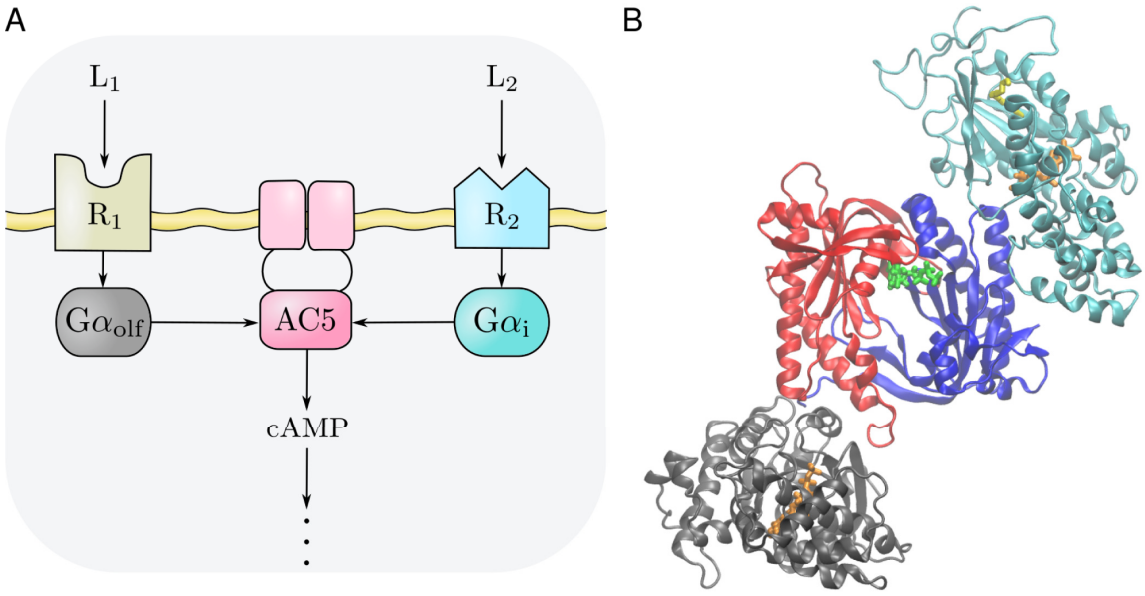

Fig 1. **A** General scheme of the AC5 signal transduction network. It applies to both the D_1 and D_2 MSNs discussed in the text. Two agonists (L_1 and L_2) bind to two GPCRs (R_1 and R_2), releasing the $G\alpha_{olf}$ and $G\alpha_i$ subunits, respectively. These stimulate and inhibit the conversion of cAMP, respectively. **B** Initial modelled configuration of the $G\alpha_{olf} \cdot AC5 \cdot G\alpha_i$ ternary complex, used in the classical MD simulations. The cytosolic part of the AC5 enzyme consisting of the pseudo-symmetric C1 (blue) and C2 (red) cytoplasmic domains in an ATP-bound (green) conformation are complexed to an active conformation of $G\alpha_{olf}$ (gray) and to $G\alpha_i$ (cyan). GTP (orange) and the myristoyl moiety in $G\alpha_i$ (yellow) are shown in stick representation. Controlling the relative positions and conformations of C1 and C2 may enhance or inhibit enzymatic function. This is one way in which $G\alpha_{olf}$ and $G\alpha_i$ exert their regulatory effects: each of them has a separate binding site on the AC5 domain dimer.

https://doi.org/10.1371/journal.pcbi.1007382.g001

whether AC5 is a coincidence detector will help us understand if and why changes in more than one of the neuromodulatory signals it receives are necessary to trigger synaptic plasticity. This is what we have set out to determine in this study. We use the neuromodulation of D_1 MSNs as the example here (see [15]).

Recent quantitative estimates of the efficacy of ACh on M_4 receptors in D_1 MSNs suggest that the basal ACh level (even a few tens of nanomolars), resulting from the tonic activity of cholinergic interneurons, may produce $G\alpha_i$ activation [14]. The active $G\alpha_i$ could be sufficient to tonically inhibit significant amounts of AC5 under baseline conditions. In addition, it has been proposed that the dopamine-dependent D_1 activation of AC5 by $G\alpha_{olf}$ is quite low at baseline conditions [19]. This partly inhibited state of AC5 could be considered as the "resting state" of striatal AC5 signaling. Previous modeling studies of this signal transduction network predicted that AC5 responds most strongly to a simultaneous increase in dopamine (Da↑) and a pause in acetylcholine levels (ACh↓), i.e. both stimulation by increased $G\alpha_{olf}$ and disinhibition by decreased $G\alpha_i$ are necessary for the enzyme to produce significant amounts of cAMP [15]. The response to the two neuromodulatory signals was nonlinear and synergistic. This suggests that AC5 might function as a coincidence detector, since the network responds with significant amounts of cAMP only when the two incoming signals Da↑ and ACh↓ coincide in time and in the spatial vicinity of the receptors. In order to perform strong coincidence detection, the network should be able to make a clear distinction between the situation of a simultaneous dopamine peak and acetylcholine dip (Da↑ + ACh↓) and that of a single signal, i.e. Da↑ or ACh↓ alone. This distinction is realized by producing different amounts of cAMP, i.e. by differences in the enzyme's catalytic rate.

During the course of our previous kinetic modelling study [15], and follow-up experimental studies on the function of the AC5 signal transduction network [14,19], it became clear that the presence or absence of a ternary $G\alpha_{olf} \cdot AC5 \cdot G\alpha_i$ complex during AC5 regulation, and the level of catalytic activity of such a complex, could significantly affect AC5's ability to act as a coincidence detector.

While the existence of the binary $AC5 \cdot G\alpha_i$ and $AC5 \cdot G\alpha_{olf}$ complexes, and their catalytic activities, has been confirmed experimentally, a $G\alpha_{olf} \cdot AC5 \cdot G\alpha_i$ ternary complex has not been identified so far [20–22]. However, it has been suggested to exist during AC5 regulation, but it is not known whether it would be catalytically active or inactive (Fig 1B) [21, 23]. So far, we know from molecular dynamics (MD) simulations of the binary complexes that binding of one Gα subunit can produce allosteric effects at the binding site for the other [24,25], raising the speculation that allosteric effects influence ternary complex formation.

Resolving the details of AC5 regulation can help to understand whether AC5 acts as a coincidence detector, and hence, whether transient changes in two neuromodulatory signals are necessary for plasticity and learning in the basal ganglia. Here, we take a multiscale modeling approach to address the following question: can the $G\alpha_{olf} \cdot AC5 \cdot G\alpha_i$ ternary complex form in the AC5 signal transduction network? If it does, is it able to catalyse ATP conversion, and does its presence affect the ability of the enzyme to perform coincidence detection? We combine MD simulations, to study the complexation of AC5 with its Gα partners, with Brownian dynamics (BD) simulations to estimate the forward (association) rate constants of binding between AC5 and the Gα subunits. Snapshots from the MD simulations are used as starting points for BD simulations. We then incorporate the results from these simulations into a kinetic model of the AC5 signal transduction network and quantify the ability of the enzyme to detect coincident extracellular signaling events. Molecular simulation approaches that bridge multiple spatial and temporal scales are well established [26], and here we span the spatial scales by bridging from intra- and inter-molecular dynamics up to the function of a biochemical reaction network [27,28,29]. Multiscale simulation is particularly informative for this system since experimental efforts in studying the ternary complex have not yielded results.

Our MD simulations show that a ternary complex could be present during AC5 regulation, being stable on the μs timescale, but it appears to be catalytically inactive. The kinetic model, constructed using results from the MD and BD simulations performed here, reveals that: (i) the suggested interaction scheme between the regulatory Gα subunits and AC5 strengthens coincidence detection when compared to alternative schemes; (ii) the predicted values of the forward rate constants are favourable for coincidence detection. This suggests that AC5 is indeed a powerful coincidence detector and, as a result of the inactive ternary complex, a rise in dopamine alone does not have an effect on synaptic plasticity; it needs to be accompanied by a pause in the level of acetylcholine. These insights are also discussed with regard to other AC isoforms.

Results

Molecular dynamics simulations indicate that the apo $G\alpha_{olf} \cdot AC5 \cdot G\alpha_i$ ternary complex is stable on microsecond timescales

The existence of a ternary complex, $G\alpha_{olf} \cdot AC5 \cdot G\alpha_i$, during AC5 regulation has been unclear. So far it has not been possible to detect the complex in experiments, possibly due to its unstable nature [21]. However, as $G\alpha_{olf}$ and $G\alpha_i$ interact with AC5 on different sites on its catalytic domains, the ternary complex could be formed via two reactions:

$$AC5 \cdot G\alpha_i + G\alpha_{olf} \leftrightarrow G\alpha_{olf} \cdot AC5 \cdot G\alpha_i, \text{ and}$$

$$AC5 \cdot G\alpha_{olf} + G\alpha_i \leftrightarrow G\alpha_{olf} \cdot AC5 \cdot G\alpha_i.$$

Previous MD simulation results suggested that upon binding of $G\alpha_i$ to AC5, the $G\alpha_{olf}$ binding groove adopts a conformation that hinders $G\alpha_{olf}$ from binding [24], making the first reaction less favourable; however, a stable ternary complex might still be formed via the second route. All-atom MD simulations were employed to investigate the stability of a putative *apo* ternary complex, $G\alpha_{olf} \cdot AC5 \cdot G\alpha_i$, in the absence of ATP, on the μs time scale. We mention here that $G\alpha_{olf}$ has no post-translational modifications to its protein sequence. In contrast, $G\alpha_i$ is considered in its myristoylated form since a non-myristoylated $G\alpha_i$ subunit is known to be unable to form an $AC5 \cdot G\alpha_i$ complex and, therefore, it is not functional [21, 24].

The *apo* ternary complex appears to be stable over the course of 2.1 μs of all-atom MD simulation with a root-mean-square deviation (RMSD) of the complex's backbone fluctuating between 0.8 and 1 nm (Fig 2B) compared to the first frame of the trajectory. The RMSD of each individual protein, i.e. AC5, $G\alpha_{olf}$ or $G\alpha_i$, in the *apo* ternary complex remains below 0.4 nm (S1 Fig). Similar RMSD values have been found for the *apo* forms of the binary complexes $AC5 \cdot G\alpha_{olf}$ and $AC5 \cdot G\alpha_i$ (S1 Fig). Additionally, analysis of the secondary structures and calculations of the numbers of H-bonds as functions of time for all systems confirm the overall stability suggested by the RMSD analysis (S2–S7 Figs). Root-mean-square-fluctuations (RMSF) per residue have also been calculated (S6 Fig).

Minor differences in RMSF were observed for $G\alpha_{olf}$ and $G\alpha_i$, independently of the simulated system. Conversely, in the case of AC5, the C2 β4'-β5' region (i.e. residues Val1186 to Trp1200 of the C2 domain) and the C2 β7'-β8' region (i.e. residues Gln1235 to Asn1256 of the C2 domain) show a change in orientation dependent on the presence of the Gα subunit. Whereas β7'-β8' appears to be more flexible in the binary $AC5 \cdot G\alpha_{olf}$ complex, the β4'-β5' region is more flexible in the presence of $G\alpha_i$. Besides RMSD, a measure of compactness of the simulated complexes is provided by the global radius of gyration (R_g), which also provides an indication of the stability of the complex. R_g was calculated as a function of time along the simulated trajectories for all three complexes (S7 Fig). In the case of the *apo* $AC5 \cdot G\alpha_i$ complex, a

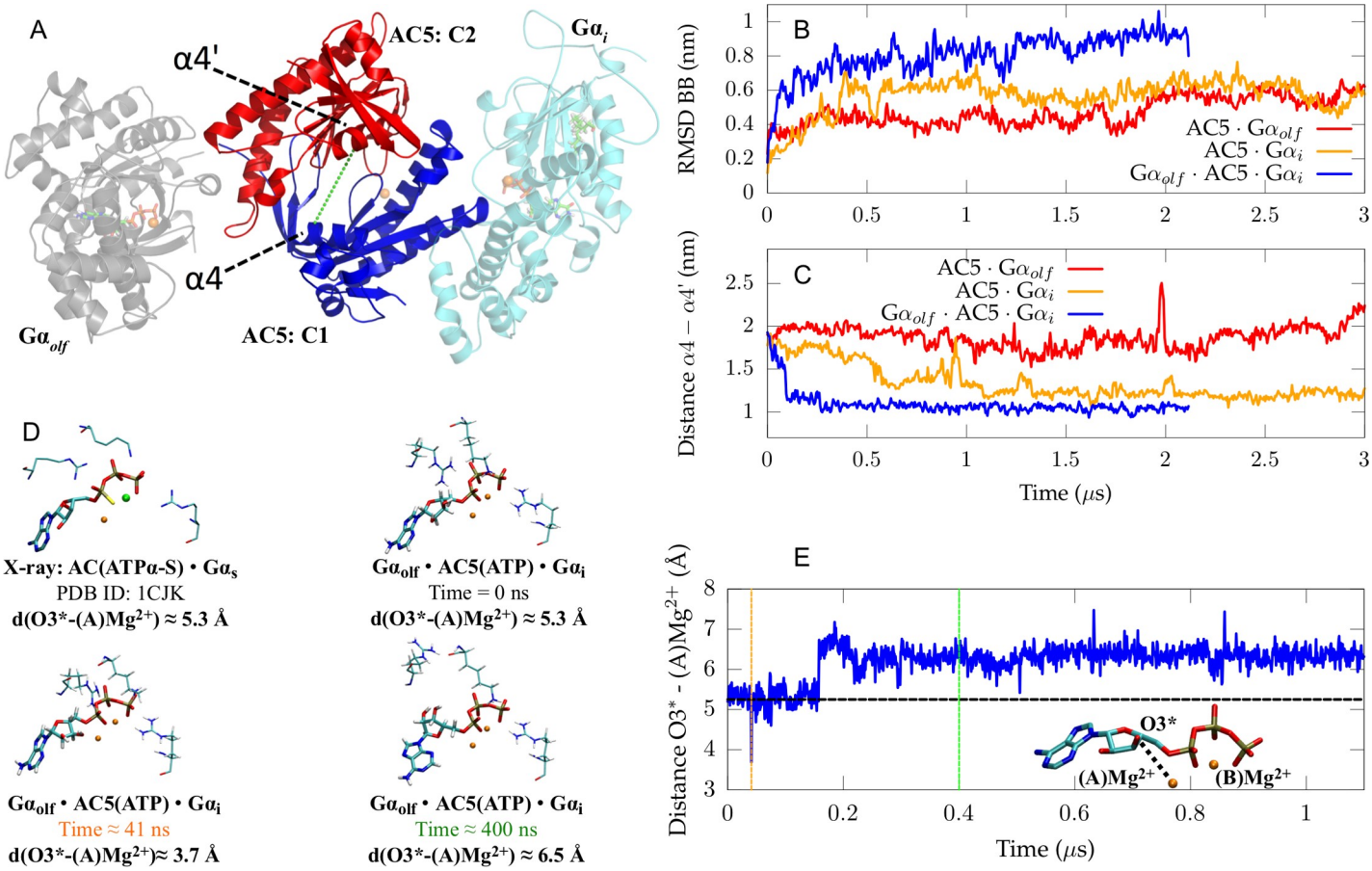

Fig 2. Stability analysis of the *apo* ternary complex, conformation of the active site of AC5 in the *apo* state, and conformation of ATP in AC5's active site in the *holo* state. A Initial conformation of the *apo* ternary complex including $G\alpha_{olf}$ (gray), $G\alpha_{i1}$ (cyan), C1 (blue), C2 (red). In addition to the protein structures, two GTP molecules as well as the myristoyl moiety of the $G\alpha_{i1}$ subunit and three Mg^{2+} ions are shown. The green dashed line indicates the distance between the Cα atom of Thr1007 (belonging to helix α4) and the Cα atom of Ser1208 (belonging to helix α4'). **B** RMSD of the backbone of the protein complexes $G\alpha_{olf}$ · AC5 · $G\alpha_{i1}$, AC5 · $G\alpha_{olf}$ and AC5 · $G\alpha_{i1}$. **C** Time evolution of the distance between Thr1007 and Ser1208 for the three simulated complexes in *apo* form. **D** Conformation of ATP in the $G\alpha_{olf}$ · AC5(ATP) · $G\alpha_{i1}$ system at different time intervals in the trajectory as well as the conformation of ATPα-S in the AC · $G\alpha_s$ X-ray structure (PDB code 1CJK). The color of the time in green and orange corresponds to the coloured lines in image (E). **E** Distance between the oxygen of a hydroxyl on the sugar ring of ATP, $O3^*$, and a Mg^{2+} ion, (A) Mg^{2+}, in the active site of the *holo* ternary complex. The black dashed line shows the distance between the two atoms in the AC · $G\alpha_s$ X-ray structure (PDB ID 1CJK) to which ATPα-S is bound [22].

https://doi.org/10.1371/journal.pcbi.1007382.g002

clear reduction of R_g can be observed compared to its initial conformation. The *apo* form of AC5 · $G\alpha_{olf}$ also shows a reduction of R_g over time, while R_g increases for the *apo* ternary complex system with respect to the starting value. In this regard, it is worth pointing out that after the first 500 ns, R_g does not increase further and, instead, oscillates around a constant value, slightly higher than that for the first frame. Such behaviour does not suggest instability of the ternary complex, but is rather an indication of an initial reorientation of the different domains to optimize their interaction. Such structural rearrangement is not surprising considering that the initial structure of the ternary complex was generated by homology modelling.

Simulations of the *apo* and *holo* state of the ternary complex indicate that it is unable to catalyse ATP conversion

To assess the ability of the ternary complex to catalyse the conversion of ATP to cAMP, we investigated the structural dynamics of the ATP binding site during the MD simulation of the

apo ternary complex, and the conformations sampled by ATP in a simulation of the *holo* ternary complex, $G\alpha_{olf} \cdot AC5 \cdot G\alpha_i$ in which ATP is bound to the active site of AC5. We compare the conformational changes of the proteins in the *apo* ternary complex with those in the previously reported simulation of the *apo* $AC5 \cdot G\alpha_i$ complex [24] and with those of the *apo* $AC5 \cdot G\alpha_{olf}$ simulation reported here.

The ability of AC5 to convert ATP to cAMP depends on the state of its catalytic domain. A characteristic quantity in this respect is the relative distance between the two helices α4' and α4 positioned either side of the binding groove (Fig 2A). The distance between the Cα atom of Thr1007 in helix α4 and the Cα atom of Ser1208 in helix α4' (highlighted by the green dashed line in Fig 2A) was calculated along the simulated trajectories for the three complexes investigated here and reported as a function of time in Fig 2C.

This distance exhibits a clear decrease in the first 100 ns in the $G\alpha_{olf}$· $AC5 \cdot G\alpha_i$ complex, starting from a value of 1.9 nm and reaching a stable value of about 1.1 nm. Similarly, a decrease of the α4-α4' distance was also observed in the $AC5 \cdot G\alpha_i$ complex along 3 μs of simulation. Conversely, when AC5 is bound to $G\alpha_{olf}$ in a binary complex, the distance between the two helices is characterized by a higher value with respect to the case of the $AC5 \cdot G\alpha_i$ and $G\alpha_{olf}$· $AC5 \cdot G\alpha_i$ complexes. A larger value of this distance can be associated with a higher accessibility of the binding groove. On the other hand, a reduced value, as found in the AC5 domain bound to $G\alpha_i$ implies a lower accessibility to the binding groove. The effect of the reduction in α4-α4' distance on active site conformation and residue orientation has been described in [24] for the $AC5 \cdot G\alpha_i$ complex. A shorter distance between the α4 and α4' helices decreases the volume in the active site accessible to ATP as α4' starts occupying the region in which ATP's adenine moiety docks. Due to the conformational changes in the active site, important residues for ATP stabilization undergo a rearrangement in orientation that appear to significantly differ from the $AC5 \cdot G\alpha_{olf}$ system, potentially negatively impacting the probability of ATP association. Hence, this partial closure of the active site of AC5 in $AC5 \cdot G\alpha_i$ and $G\alpha_{olf} \cdot AC5 \cdot G\alpha_i$ reduces the space available for ATP binding and could also lower the probability of stable ATP association, suggesting that the ternary complex is likely to be inactive.

Apart from the ability of the *apo* ternary complex to bind the substrate, we additionally investigated the possible catalytic activity of a *holo* $G\alpha_{olf} \cdot AC5 \cdot G\alpha_i$ complex. ATP has to undergo a cyclisation reaction in order to form the products cAMP and pyrophosphate. This reaction is induced by the attack of a deprotonated hydroxyl moiety in ATP's sugar ring, $O3^*$, on the phosphorus atom of the α-phosphate moiety (Fig 2E). Hence, ATP conversion requires oxygen $O3^*$ to be in the proximity of $(A)Mg^{2+}$ to which the phosphorus atom is coordinated in order to obtain a conformation that can undergo the cyclisation reaction [30–32].

A crystal structure of the *holo* AC domain dimer in complex with a stimulatory Gα subunit [22] shows the active conformation of ATPα-S, an ATP mimic, in the active site of the enzyme in the presence of a Mg^{2+} ion and a Mn^{2+} ion (Fig 2D), which is assumed to be substituted by a second Mg^{2+} ion under physiological conditions. The $O3^*$-$(A)Mg^{2+}$ distance in the X-ray structure of the *holo* $AC \cdot G\alpha_s$ complex is 5.25 Å (Fig 2D). In the MD trajectory of the *holo* ternary complex, the $O3^*$-$(A)Mg^{2+}$ distance starts at a similar value and mainly remains in this state for the first 160 ns. Within the first 160 ns, the $O3^*$-$(A)Mg^{2+}$ distance even decreases to distances as short as 3.7 Å, closer to the distance which has been suggested to correspond to ATP's reactive state [30–32] (see orange line). However, after 160 ns, the ATP molecule undergoes a drastic conformational change, resulting in an increase of the $O3^*$-$(A)Mg^{2+}$ distance to ≈6.5 Å. In this state, the ATP molecule is unable to attain a short $O3^*$-$(A)Mg^{2+}$ distance, such as observed at 41 ns, which is a feature of the reactive state of ATP. This conformational transition of ATP appears to be irreversible on the μs time scale, thus suggesting the inhibition of the catalytic reaction.

The rate of diffusional association of each Gα protein subunit to AC5 is unaffected by prior binding of the other subunit

To provide initial values for the forward rate constants - the parameters in the kinetic model of AC5 activity which were not constrained experimentally - we performed BD simulations (Table 1). The predicted rate constants suggest both Gα subunits form complexes at similar rates, and their association is not greatly affected by the presence of ATP in the AC5 active site, or prior binding of the other subunit. Indeed, the variation in the predicted rate constants for each reaction across the different MD snapshots used in BD simulations is greater than the variation of the mean values for each constant (S1 Table).

It should be noted that the predicted rate constants are for the diffusional approach and initial binding of the Gα subunits to AC5. The previously reported MD simulations show that the binding of $G\alpha_{olf}$ to AC5 · $G\alpha_i$ is hindered by a conformational change of its binding groove on AC5, adding an additional conformational gating contribution to the rate of binding that is not described by the BD simulation method used [24].

The presence of an inactive ternary complex improves the ability of the network to detect coincident signals

We incorporated the results from the MD and BD simulations into a kinetic model of the AC5 signal transduction network, the basic feature of which is a regulatory scheme where the ternary complex can form (Fig 3C). We find that this network can perform coincidence detection. To investigate how the ternary complex contributes to the network's ability to perform coincidence detection, we compared the system with a network in which no ternary complex can form.

It is important to note that there are two aspects of coincidence detection: (a) distinguishing between the different inputs, and (b) responding strongly enough with an increase in cAMP concentration that is physiologically relevant. As a proxy for the amount of cAMP produced, we use the average catalytic rate of AC5, k_c, since the amount of cAMP produced is proportional to k_c (see Methods, and also illustrated in Fig 3). The average catalytic rate of AC5 is a weighted average of the catalytic rates of the unbound enzyme and each of the complexes with the Gα subunits. Additionally, to measure whether the signal transduction network distinguishes between the different input situations, the synergy quantity, S, is employed. This describes how much greater the average catalytic rate is when both signals coincide compared to the cases when only one of them arrives (see Methods). A synergy value greater than 1 indicates that the network can perform coincidence detection, i.e. the network responds more strongly when the two signals coincide than if each of them occurs individually and are summed. A value of 1, or less than 1, marks a response equal to or weaker than the sum of the individual signals, respectively. In these cases, the average catalytic rate does not produce distinguishable amounts of cAMP that enable the cell to discriminate between the different input

Table 1. Bimolecular association rate constants (nM-1s-1) for the forward reactions computed from BD simulations (standard deviation over all structures of complexes and replica simulations shown in parentheses). Rate constants were calculated separately for complexes incorporating both apo and holo AC5. Data for each individual structure of each complex are shown in S1 Table.

Rate Constant	*apo* AC5	*holo* AC5
k_{f1}	0.018 (0.007)	0.026 (0.009)
k_{f2}	0.02 (0.01)	0.05 (0.01)
k_{f3}	0.012 (0.008)	0.017 (0.006)
k_{f4}	0.02 (0.01)	0.020 (0.006)

https://doi.org/10.1371/journal.pcbi.1007382.t001

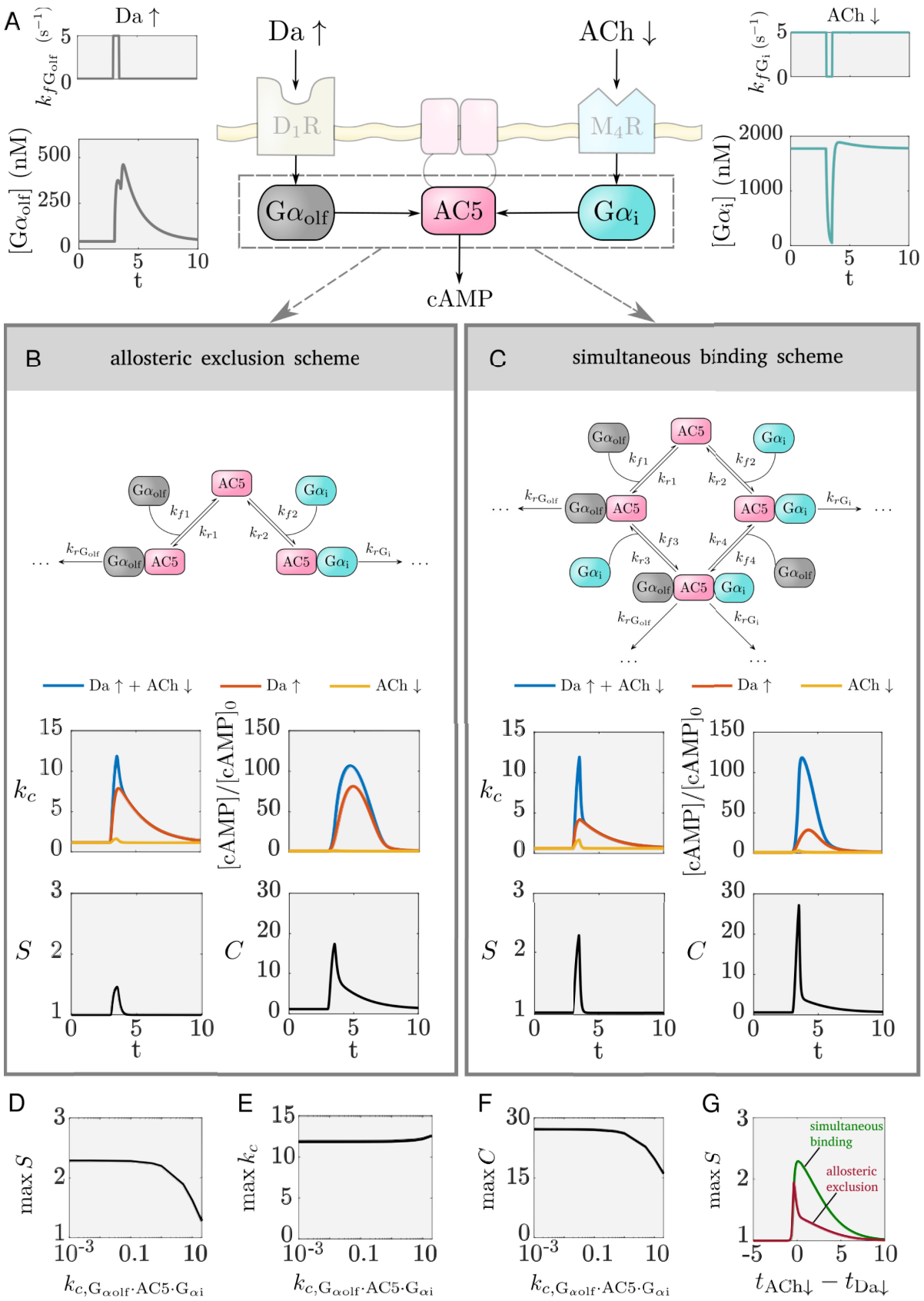
A
Da ↑
ACh ↓
D1R
M4R
Gαolf
AC5
Gαi
cAMP
[Gαolf] (nM)
[Gαi] (nM)
t
B allosteric exclusion scheme
C simultaneous binding scheme
Da ↑ + ACh ↓
Da ↑
ACh ↓
kc
[cAMP]/[cAMP]0
S
C
D
E
F
G
max S
max kc
max C
simultaneous binding
allosteric exclusion
tACh↓ − tDa↓

Fig 3. The effect of the different regulatory schemes on coincidence detection. A The inputs to the model translate to an elevation in $G\alpha_{olf}$ and pause in $G\alpha_i$. The shaded parts of the scheme are not included in the kinetic model. **B** The allosteric exclusion scheme, and the k_c, synergy, and cAMP levels obtained due to this regulatory scheme. **C** The simultaneous binding scheme, and the k_c, synergy, and cAMP levels obtained due to this regulatory scheme. **D,E,F** The effect of the ternary complex' catalytic activity on coincidence detection: the maximum of the synergy (D), the maximum of k_c (E), the maximum of the metric C (F). **G** The detection window for the allosteric occlusion scheme (red) and the simultaneous binding scheme (green). $t_{Da}\uparrow$ and $t_{ACh}\downarrow$ are the times when the Da↑ and ACh↓ occur, respectively. Note the shared time axes in (A), (B) and (C).

https://doi.org/10.1371/journal.pcbi.1007382.g003

situations. Since a synergy greater than 1 does not necessarily indicate a strong response from the network (i.e. strong cAMP production), a combination of the average catalytic rate and the synergy is applied where needed to quantify coincidence detection (see the metric C in methods).

The regulatory schemes that we compare are given in Fig 3B and 3C. We name the first scheme an *allosteric exclusion scheme* – the binding of one Gα subunit excludes the possibility for binding of the other Gα subunit. The second scheme is termed the *simultaneous binding scheme*, where both Gα subunits can bind to AC5 and the ternary complex can be formed. Simulation results for both schemes are given in Fig 3. The inputs are assumed to be a dopamine peak of 0.5s (Da ↑) and an acetylcholine dip of 0.5s (ACh ↓), and the corresponding rise in $G\alpha_{olf}$ and drop in $G\alpha_i$ are shown in Fig 3A. Time courses showing the amounts of all AC5 species (the free enzyme and the complexes with the Gα) are given in S9 Fig.

The simultaneous binding scheme can better distinguish between Da ↑ + ACh ↓ and the individual signals Da ↑ or ACh ↓, it has higher synergy. Both the schemes have a similar maximal k_c(Da ↑ + ACh ↓), and, as evident, the increase in synergy in the simultaneous binding scheme versus the allosteric exclusion scheme comes from a reduced k_c(Da ↑). This relative difference in the average catalytic rate enables the simultaneous binding scheme to respond differently to the coincident signal, Da ↑ + ACh ↓, compared to Da ↑ alone, as is also visible from the amounts of cAMP produced, and hence to differentiate between the two input situations. The allosteric exclusion scheme, on the other hand, produces similar values for k_c(Da ↑ + ACh ↓) and k_c(Da ↑) and thus responds similarly to Da ↑ + ACh ↓ and to Da ↑ alone, being unable to distinguish well between them in terms of cAMP production. The reason for this is the exclusivity of the interaction between each of the Gα proteins and AC5: when only Da ↑ arrives, $G\alpha_{olf}$ is able to compete with $G\alpha_i$ and bind to much of the enzyme (approximately half of it as shown in S9B Fig). This creates the catalytically active complex AC5 · $G\alpha_{olf}$, driving an increase in k_c(Da ↑). In this case, reduced inhibition of AC5 by an additional ACh ↓ does not contribute much to k_c(Da ↑ + ACh ↓). In the simultaneous binding scheme, however, a Da ↑ causes the formation of the ternary complex S9F Fig), and due to its inactivity k_c(Da ↑) does not increase significantly. Only with an additional ACh ↓ is the inhibition by $G\alpha_i$ relieved and the proportion of the active complex AC5 · $G\alpha_{olf}$ is increased, enabling a high k_c(Da ↑ + ACh ↓). Importantly, k_c(Da ↑) is also low for an inactive ternary complex so that little cAMP is produced with a Da ↑ only and little "stray" activation of downstream signalling would occur. In fact, only for a substantially active ternary complex does the simultaneous binding scheme become comparable to the allosteric exclusion scheme in terms of synergy (Fig 3D, 3E and 3F). For a wide range of low to moderate ternary complex activity, it performs coincidence detection better. The maximum of the catalytic rate is not affected much by the activity of the ternary complex (Fig 3E), and the metric C shows that coincidence detection is most significant for an inactive ternary complex (Fig 3F). An inactive ternary complex enables the lowest catalytic activity of the enzyme at resting state and hence the biggest difference between k_c(Da ↑) and k_c(Da ↑ + ACh ↓), and this in turn maximizes the synergy.

In the supplementary material we show that the allosteric exclusion scheme in itself lacks the ability to perform coincidence detection, and this is due to the exclusivity of the regulatory

interaction. Coincidence detection with this scheme, as demonstrated in Fig 3B, is in fact a result of the amounts of $G\alpha_{olf}$ and $G\alpha_i$ and the kinetics determined by the forward rate constants.

An inherent property of a coincidence detector is that there exists a time window over which two signals can be detected as if arriving together. The detector uses some mechanism by which it "remembers" the occurrence of one of the signals for some time interval, and responds when the other signal arrives within this interval. For the AC5 signal transduction network, the existence of the detection window also depends on the regulatory scheme. In fact, the formation of the ternary complex is very important to allow for a broader window of coincidence detection. In the case of only a Da↑, a ternary complex that has buffered (or absorbed) the elevated active $G\alpha_{olf}$ provides this memory: allowing the ACh↓ to arrive some time later and still elicit a response (Fig 3G). This is potentially relevant, since the cholinergic interneurons responsible for the ACh↓ have been found to produce a second ACh↓ to certain stimuli [33]. The length of the detection window is determined by the rate of deactivation of the active $G\alpha_{olf}$ (also illustrated in S10D and S10G Fig, and is due to the fact that the GTPase activity for $G\alpha_{olf}$ is lower than the one for $G\alpha_i$). Both schemes technically have the same length of detection windows, but the allosteric exclusion scheme has a high synergistic effect in a very narrow region of the window - the signals need to occur practically simultaneously (Fig 3G). The detection window is asymmetric, i.e. the Da↑ needs to arrive first to elicit a response from the network. (Time courses with ACh↓ preceding and following a Da↑ illustrating the difference between the two schemes are given in S10 Fig.)

Lastly, we note that a critical aspect for coincidence detection to work is to have fast deactivation of the active $G\alpha_i$. Then the dynamics of $G\alpha_i$ inside the cell can follow the short duration of the ACh↓ signal. The experimental evidence for this high GTPase rate is listed in the description of the kinetic model (see Methods). The effect of the GTPase rate on coincidence detection is shown in S11 Fig. There is an optimum value of this rate - it needs to be both high enough to cause a drop in $[G\alpha_i]$ during the ACh↓ and low enough so that there is significant inhibition of AC5 at steady state. Since the deactivation of $G\alpha_i$ is faster than that for $G\alpha_{olf}$, then, provided there is enough active $G\alpha_{olf}$ to bind to AC5, the duration of the synergistic effect is determined by the duration of the pause (S10E and S10G Fig). More extensive analysis on the robustness of coincidence detection to parameter values has been performed for the previous, much larger kinetic model of the signal transduction network [34].

To summarize, the results of this section show that the formation of the ternary complex aids coincidence detection and prolongs the detection window. Additionally, the less catalytically active the ternary complex is, the better the coincidence detection. As elaborated in the discussion, an inactive ternary complex can also explain recent experimental results on cAMP production due to activation of the implicated GPCRs in the native system [14,19].

Hindrance of $G\alpha_{olf}$ binding to AC5 · $G\alpha_i$ still allows coincidence detection

To see where the predicted values from the BD simulations lie in terms of affecting coincidence detection, we performed parameter scans for the values of the forward rate constants. All of the forward rate constants affect the synergy, since they affect the fractions q_i, i = 1, . . ., 4, of each species at any point in time (see equations for q_i in Methods).

To begin with, we address the observation from Van Keulen and Röthlisberger [24] that the $G\alpha_{olf}$ binding groove in AC5 · $G\alpha_i$ adopts a conformation that hinders $G\alpha_{olf}$ binding. This could further decrease the value of the rate constant k_{f4}, compared to the value predicted in the BD simulations. We investigated the effect such a decrease has on coincidence detection by altering k_{f4} by varying orders of magnitude (Fig 4A, 4B and 4C). We found that hindered

binding of $G\alpha_{olf}$ to AC5 · $G\alpha_i$ does not affect coincidence detection significantly (the synergy S is increased by 12%). Nevertheless, when performing the parameter scans, we considered two scenarios. In the first one, we used $k_{f1} = k_{f4}$ and $k_{f2} = k_{f3}$ since the BD simulations showed that these values are similar, at least in order of magnitude. In the second scenario, we used $k_{f2} = k_{f3}$ and $k_{f4} = k_{f1}/100$. We call this scheme, in which the reaction corresponding to the rate k_{f4} is slower, the *hindered simultaneous binding scheme*.

For the simultaneous binding scheme, a very wide range of tested values for k_{f1} provides similar k_c and synergy values for a given k_{f2} (Fig 4D and 4E), which can be interpreted as follows. Similarly to the requirement for a high GTPase activity for $G\alpha_i$, it is necessary that $G\alpha_{olf}$ binds to AC5 quickly enough to be able to follow the signal Da ↑. Since active $G\alpha_{olf}$ has a slower dynamics than the input Da ↑, i.e. $G\alpha_{olf}$ exists inside the cell for some time after the outside signal has stopped, it is likely that a range of values for the rate constant k_{f1} can enable coincidence detection (not only values that match the length of a Da ↑, which are around $k_{f1} = 2\ (nMs)^{-1}$ for a Da ↑ of 0.5s). The synergy grows with k_{f1} since a higher binding rate of $G\alpha_{olf}$ provides a higher maximum of k_c during the Da ↑ + ACh ↓, whereas k_c(Da ↑) is not affected much (S12A and S12B Fig).

Increasing the rate constants $k_{f2} = k_{f3}$ for $G\alpha_i$ binding also causes an increase in synergy. The lower these constants, the less inhibited the enzyme will be due to smaller fractions of both AC5 · $G\alpha_i$ and $G\alpha_{olf}$ · AC5 · $G\alpha_i$. This allows for more stimulation by the available $G\alpha_{olf}$ and hence a higher resting-level k_c and a higher k_c(Da ↑). The situations Da ↑ + ACh ↓ and only Da ↑ produce a more similar response, and hence show a lower synergy. Higher values for $k_{f2} = k_{f3}$, on the other hand, allow for both stronger resting-level inhibition of AC5 and more ternary complex formed, and hence a lower resting-level k_c and lower k_c(Da ↑), thus increasing the synergy. The region of optimal parameters for the simultaneous binding scheme is quite wide in terms of $k_{f1} = k_{f4}$ and $k_{f2} = k_{f3}$, and the most optimal scenario is for the largest values tested, as shown in Fig 4F using the metric *C*.

Compared to the simultaneous binding scheme, the hindered simultaneous binding scheme does not affect the maximum of the average catalytic rate significantly (Fig 4H), but it moves the region of optimal values for the synergy towards low values for the rate constant k_{f1} and increases it for these values (Fig 4G). Inspecting the dynamics of the model with this regulatory scheme reveals the reason: the hindered reaction AC5 · $G\alpha_i$ + $G\alpha_{olf}$ ↔ $G\alpha_{olf}$ · AC5 · $G\alpha_i$ causes less ternary complex to be formed and consequently less AC5 · $G\alpha_{olf}$ from the dissociation of $G\alpha_i$ from the ternary complex (the route via k_{r3}) (S12C and S12D Fig). This, in general, lowers k_c(Da ↑) compared to the simultaneous binding scheme, creating a larger relative difference between k_c(Da ↑) and k_c(Da ↑ + ACh ↓) which results in a high synergy. This difference is largest for low values of k_{f1} and decreases with k_{f1} due to the higher amounts of AC5 · $G\alpha_{olf}$ during the Da ↑ (higher k_c(Da ↑)). Importantly, the maximal k_c has the opposite dependence on k_{f1} from the synergy, so that the region of values for k_{f1} optimal for coincidence detection optimizes between a high catalytic rate and a high synergy (Fig 4I). The effect of $k_{f2} = k_{f3}$ on coincidence detection is the same as described for the simultaneous binding scheme.

In both scenarios, the predictions of the BD simulations are favourable for coincidence detection. However, higher binding rates of $G\alpha_i$ than the predicted ones are better suited for coincidence detection. This increase in k_{f2} and k_{f3} could arise if $G\alpha_i$ were part of multiprotein signaling complexes, as has been shown for AC5 and $G\alpha_{olf}$ [35–37].

Discussion

In this study we find that an inactive ternary complex between AC5 and its G protein regulators, a molecular-level feature, gives rise to significantly increased coincidence detection, a

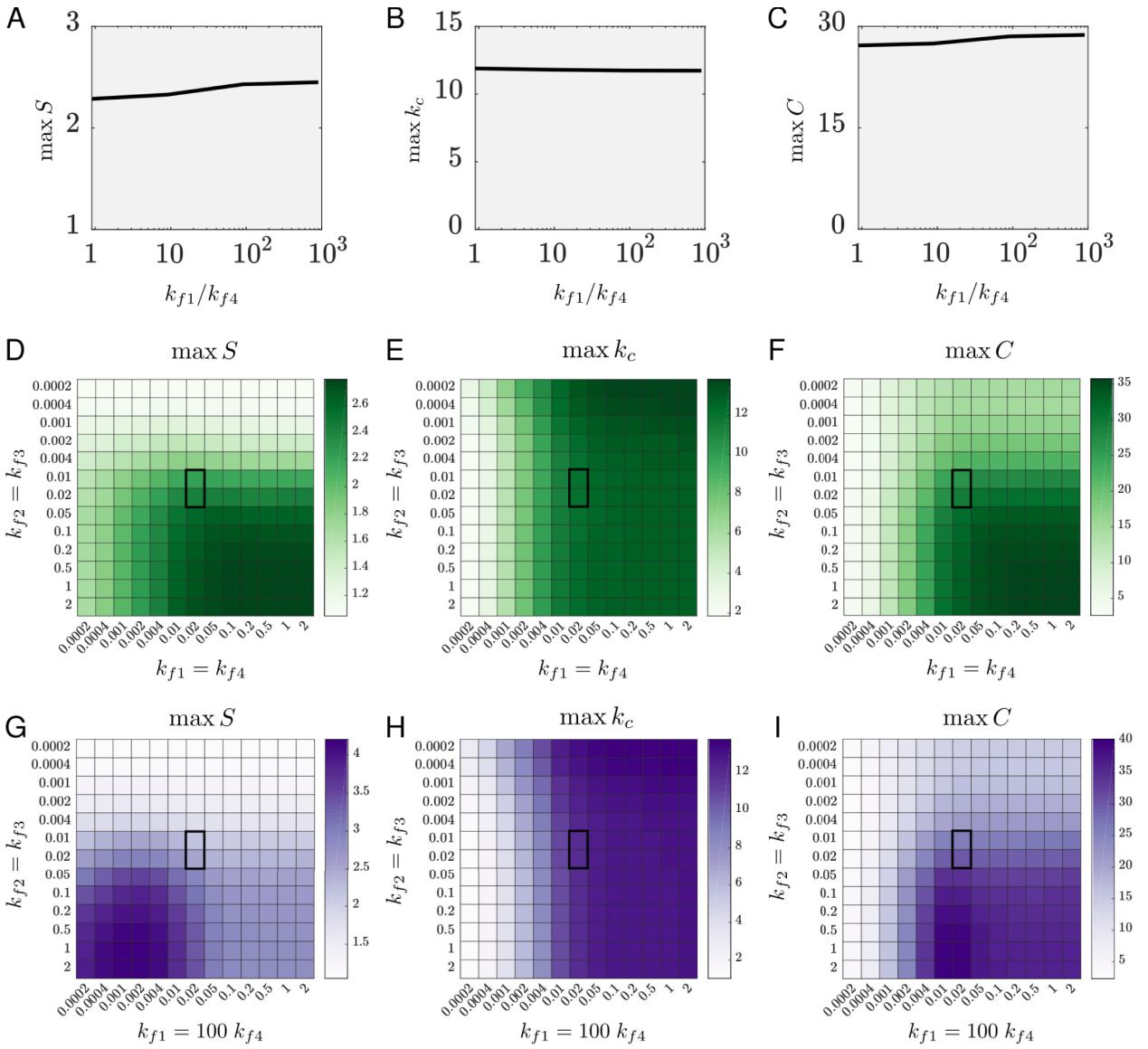

Fig 4. Dependence of coincidence detection on the forward rate constants. A, B, C The maximum of the synergy (A), the maximum of k_c (B) and the maximum of the metric C (C) for a reduced rate constant k_{f4} relative to the prediction from BD simulations. **D, E, F** Coincidence detection for the simultaneous binding scheme as dependent on the forward rate constants: maximum of the synergy (D), maximum of k_c (E), maximum of the metric C (F). **G, H, I** Coincidence detection for the hindered simultaneous binding scheme as dependent on the forward rate constants: maximum of the synergy (G), maximum of k_c (H), maximum of the metric C (I). Axes are in units of $(nMs)^{-1}$. Highlighted regions correspond to the forward rate constants predicted from BD simulations.

https://doi.org/10.1371/journal.pcbi.1007382.g004

systems-level function of the signal transduction network that AC5 is embedded in. In order to investigate the stability and the activity of the putative $G\alpha_{olf} \cdot AC5 \cdot G\alpha_i$ ternary complex, we carried out all-atom MD simulations. Our results showed that on the μs time scale, the complex seems to be stable independently of the presence or absence of ATP. Additionally, previous MD studies suggest possible pathways for the formation of the ternary complex, showing the possibility of the $G\alpha_i$ protein to bind to the *holo* $AC5 \cdot G\alpha_s$ complex [25], and disfavoring the binding of $G\alpha_{olf}$ to the *apo* $AC5 \cdot G\alpha_i$ complex [24]. Overall, it should be pointed out that MD simulations cannot exclude the instability of the ternary complex on longer time

scales, which cannot be assessed due to computational limits. However, MD simulations can help us to investigate the conformations sampled by the ternary complex at physiological temperature and pressure and, consequently, the activity of the complex. Indeed, the partial closure of the binding groove found in the *apo* ternary complex, analogous to that occurring in the binary *apo* AC5 · $G\alpha_i$, suggests a lack of catalytic activity in the ternary complex due to the reduced accessibility for the ATP substrate. Additionally, even if a ternary complex could exist with ATP bound to AC5, our results show that the substrate would adopt a conformation not suitable for the subsequent catalytic reaction leading to the formation of cAMP. It is worth mentioning that possible conformations sampled by ATP, prior and during its conversion to cAMP, have been reported by Hahn et al. in a theoretical study [38]. Such conformations, required for an optimal conversion of ATP to cAMP, clearly show an opposite orientation of the oxygen $O3^*$ with respect to that sampled in our simulation, thus supporting our hypothesis about the inactivity of the ternary complex.

Experimentally, indirect data exist that are consistent with a significantly inactived ternary complex. To begin with, the existence of functional oligomeric complexes of AC5 and the A_{2a} and D_2 receptors has been demonstrated, and their proposed spatial arrangement, importantly, supports ternary complex formation [39]. Additionally, experimental results from striatal cultures in this study show that stimulating the D_2 receptor almost entirely counteracts the effects of the applied agonist on the A_{2a} receptor in terms of cAMP production. These results are consistent with an inactive ternary complex since, under these conditions, both active $G\alpha_{olf}$ and active $G\alpha_i$ would exist in the cell, and activation of $G\alpha_i$ stops the activity of the previously formed AC5 · $G\alpha_{olf}$. Similar experimental studies with the *in vitro* native system have also been performed recently [14,19], although the animals used in these studies are very young (between 7 and 12 days old) and the developmental transition from AC1 to AC5 in the striatum is not complete. However, at P7 AC5 contributes to at least 50% of the cAMP response, and this contribution significantly increases further on, as the transition is reported to be complete by P14 [40]. Comparison with these experimental results is therefore still informative, and in both studies the results are consistent with an inactive ternary complex. In D_1 MSNs, stimulating the D_1 receptors with an agonist followed by activation of the M_4 receptors completely abolishes the cAMP response of AC5 [14, Fig 3A]. The analogous experiment in D_2 MSNs is also consistent with an existing and inactive ternary complex [19, Fig 2B]. Stimulating the A_{2a} receptor with an agonist and then uncaging dopamine, which stimulates the D_2 receptor, also abolishes the cAMP response. Experiments modeling the opposite regulatory effects of $G\alpha_s$ and $G\alpha_i$ on AC5 in living HEK293T cells via two other GPCRs are also consistent with an inactive ternary complex, where activation of the $G\alpha_i$ signaling branch completely reverts cAMP production due to the activated $G\alpha_s$ branch back to baseline levels [41, Fig 6A and 6B]. Earlier *in vitro* experiments with membranes of Sf9 cells expressing AC5, however, have not yielded complete inhibition by $G\alpha_i$ [23,42]. Adding high amounts of both $G\alpha_{olf}$ and $G\alpha_i$ to the assays of AC5-containing membranes did not completely inhibit AC5 - the enzyme still produced significant amounts of cAMP [23,42]. Nevertheless, a catalytically active ternary complex still supports coincidence detection for a wide range of ternary complex activity, as shown in Fig 3D–3F, as long as its catalytic rate is noticeably smaller than that of the active binary complex AC5 · $G\alpha_{olf}$. Additionally, the data in [23] are interpreted and fitted with an alternative, more elaborate interaction scheme where the ternary complex can form and is not very active, and the production of cAMP is due to higher order, catalytically active complexes of AC5 with more than one $G\alpha_{olf}$ and $G\alpha_i$ subunit. We therefore suggest that the results of our study are plausible and supported by several experimental results, among which are experiments with the native system.

Relevance for corticostriatal synaptic plasticity

Knowing what an intracellular signal transduction network is composed of and the details of how it operates can help to clarify how it responds to extracellular events. The AC5 signal transduction network in D_1 MSNs (as well as in D_2 MSNs) interacts with a calcium-activated signal transduction network to regulate synaptic plasticity. Calcium influx at the synapse is necessary for synaptic potentiation, but exerts its effect only if accompanied by activation of the AC5 signaling module [43–45]. Thus, the AC5 signal transduction network gates plasticity in the corticostriatal synapses onto the MSNs. Now, an existing and inactive ternary complex in AC5 regulation has consequences on how this "gate" would be opened: disinhibition from active $G\alpha_i$ is necessary, accompanied by stimulation from $G\alpha_{olf}$. That is, our findings suggest that the experimentally observed ACh↓ in the striatum is likely physiologically relevant for D_1 MSNs, and both a Da↑ and a ACh↓ are necessary to enable synaptic potentiation (see also [46]). They can also help in interpreting the functional role of the neuromodulatory signals in the striatum.

The kinetic model of the AC5 signal transduction network, built according to the findings of the MD simulations and with the parameters predicted with the BD simulations, reveals improved coincidence detection when compared to alternative regulatory schemes. This, together with the implications mentioned above arising from the existence and inactivity of the ternary complex, suggests that the regulation of AC5 has indeed evolved to perform coincidence detection of the two neuromodulatory signals.

Comparisons to other AC isoforms and AC-dependent cascades

In this study we have investigated the regulation of AC5 through interaction with the $G\alpha_{olf}$ and $G\alpha_i$ subunits. All membrane-bound AC isoforms are known to be stimulated by $G\alpha_s$, a close homologue of $G\alpha_{olf}$, while only ACs 1, 5 and 6 are inhibited by $G\alpha_i$ [6]. With this in mind, it is interesting to ask whether our findings concerning AC5 regulation, particularly the presence of an inactive ternary complex in the signalling network, could also be valid for cascades containing ACs 1 and 6. The sequences of rat $G\alpha_s$ and $G\alpha_{olf}$ are highly similar with an identity of 76.0% and similarity of 90.0% (S13 Fig). Restricting the comparison to the amino acid residues within 6 Å of AC5 in the modelled *apo* AC5 · $G\alpha_{olf}$ complex, the identity rises to 95.8%, with only a single position differing. For this reason, it is reasonable to assume that our findings regarding the formation of $G\alpha_{olf}$-containing complexes are also applicable to $G\alpha_s$. Indeed, our modelling of the AC5 · $G\alpha_{olf}$ complexes assumes that we can take crystal structures of AC · $G\alpha_s$ complexes as template structures. It should be noted that $G\alpha_s$ is known to be deactivated more slowly than $G\alpha_{olf}$ [47], which could reduce the ability of $G\alpha_s$-activated networks to detect subsecond coincident signals (see [34]).

Previously, we have performed electrostatic analyses of mouse AC isoforms, to identify regions of electrostatic similarity within similarly regulated isoforms [48]. In that work, we showed that the molecular electrostatic potentials surrounding ACs 1, 5 and 6 in aqueous solution were very similar in the $G\alpha_i$ binding region of AC5, suggesting that the location of binding, and the bound orientation, of $G\alpha_i$ on ACs 1 and 6, could be similar. This electrostatic similarity was due to a more negative character, compared to other AC isoforms, which is complementary to the largely positive potential of the face of $G\alpha_i$ that contains the switch II region that is thought to interact with AC.

The sequence identities of AC isoforms with respect to AC5, in the C1 domain to which $G\alpha_i$ binds, show that ACs 1 and 6 are most similar, at 73.5% and 94.7%, respectively (Fig 5B). Considering only those residues predicted to be involved in the interaction with $G\alpha_i$, the similarities are 64.7% and 91.2%. From the very high electrostatic and sequence similarity, it seems reasonable to assume that our findings should hold for AC6.

A

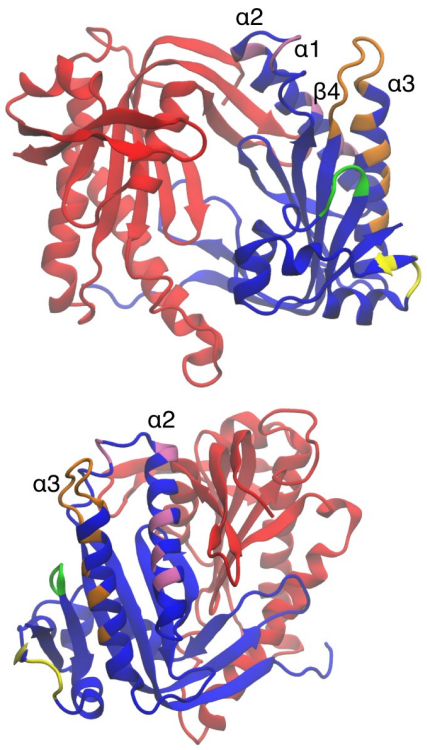

B

Isoform C1 domain	Seq. Id. AC5 C1 domain	Seq. Id. AC5 $G\alpha_{i1}$ sites
AC1	**73.5%**	**57.1%**
AC2	62.4%	50.0%
AC3	62.4%	53.6%
AC4	60.0%	46.4%
AC6	**94.7%**	**89.3%**
AC7	63.0%	53.6%
AC8	68.2%	46.4%
AC9	49.2%	32.1%

C

```
P84309  ADCY5_MOUSE     1  MMFHKIYIQKHDNVSILFADIEGFTSLASQCTAQELVMTLNELFARFDKLAAENHCLRIK  60
O88444  ADCY1_MOUSE     1  RIFHKIYIQRHDNVSILFADIVGFTGLASQCTAQELVKLLNELFGKFDELATENHCRRIK  60
                             :********:*********** ***.**********  *****.:**:**:**** ***

P84309  ADCY5_MOUSE    61  ILGDCYYCVSGLPEARADHAHCCVEMGMDMIEAISLVREVTGVNVNMRVGIHSGRVHCGV  120
O88444  ADCY1_MOUSE    61  ILGDCYYCVSGLTQPKTDHAHCCVEMGLDMIDTITSVAEATEVDLNMRVGLHTGRVLCGV  120
                            ************ : ::**********:***:**: * **.*.**:*****:*:*** ***

P84309  ADCY5_MOUSE   121  LGLRKWQFDVWSNDVTLANHMEAGGKAGRIHITKATLNYLNGDYEVEPGCGGDRNAYLKE  180
O88444  ADCY1_MOUSE   121  LGLRKWQYDVWSNDVTLANVMEAAGLPGKVHITKTTLACLNGDYEVEPGHGHERNTFLRT  180
                            *******:*********** ***.*  *::****:**  ********** * :**::*:

P84309  ADCY5_MOUSE   181  HSIETFLIL                                                   189
O88444  ADCY1_MOUSE   181  HNIETFFIV                                                   189
                            *.****:*:
```

D

```
P84309  ADCY5_MOUSE     1  MMFHKIYIQKHDNVSILFADIEGFTSLASQCTAQELVMTLNELFARFDKLAAENHCLRIK  60
Q01341  ADCY6_MOUSE     1  MMFHKIYIQKHDNVSILFADIEGFTSLASQCTAQELVMTLNELFARFDKLAAENHCLRIK  60
                           ************************************************************

P84309  ADCY5_MOUSE    61  ILGDCYYCVSGLPEARADHAHCCVEMGMDMIEAISLVREVTGVNVNMRVGIHSGRVHCGV  120
Q01341  ADCY6_MOUSE    61  ILGDCYYCVSGLPEARADHAHCCVEMGVDMIEAISLVREVTGVNVNMRVGIHSGRVHCGV  120
                           ************************:************************************

P84309  ADCY5_MOUSE   121  LGLRKWQFDVWSNDVTLANHMEAGGKAGRIHITKATLNYLNGDYEVEPGCGGDRNAYLKE  180
Q01341  ADCY6_MOUSE   121  LGLRKWQFDVWSNDVTLANHMEAGGG-RRIHITRATLQYLNGDYEVEPGRGGERNAYLKE  179
                           ************************  *****:***:*********** **:********

P84309  ADCY5_MOUSE   181  HSIETFLIL                                                   189
Q01341  ADCY6_MOUSE   180  QCIETFLIL                                                   188
                            :.*******
```

Fig 5. **A** The structure of the C1 (blue and highlight colors) and C2 (red) catalytic domains of AC5. **B** The highlighted regions show the AC5 residues that interact with $G\alpha_i$ during complex formation. Overall sequence similarity for the C1 domain for the other mouse AC isoforms, compared to mouse AC5, and for the highlighted residues that interact with $G\alpha_i$. **C, D** Pairwise sequence alignments for AC1 (C) and AC6 (D) with the colors matching those of the structure in subfigure A. The mouse sequences were taken from Uniprot, and aligned using Clustal Omega within Uniprot. The C1 domain was identified through alignment with PDB 1CJK [22], which contains a canine AC5 C1 domain, and the residues are numbered from the start of the C1 domain. The first residues of the C1 domains are at positions 288, 456 and 363 in the canonical sequences of AC1, AC5 and AC6 respectively. The red boxes in (C) indicate charge-altering substitutions between the AC5 and AC1 sequences in the $G\alpha_i$ binding α3 helix, while the blue box indicates a substitution in a residue whose mutation was found to affect $G\alpha_i$-induced inhibition of AC5 [21].

https://doi.org/10.1371/journal.pcbi.1007382.g005

While AC1 is inhibited by $G\alpha_i$, the level of inhibition is much lower, with higher levels only seen for its forskolin or calmodulin-activated states [49], therefore directly applying our findings to AC1 cascades is more difficult. In the AC1 C1 domain sequence, there are three charge-altering substitutions in the region formed by the C-terminal end of α3-helix and the loop connecting this helix to the β4-strand (Fig 5C). These substitutions give this region a more negative character, and therefore it is reasonable to assume that they should not destabilize the binding mode we find for $G\alpha_i$ on AC5 to a large extent. In a previous mutagenesis study [21], including one of these substitutions (N559D by Uniprot sequence, N480D by sequence in [21]), which is also present in the non-$G\alpha_i$ inhibited ACs 2, 4, 7 and 8 (S14 Fig), as a mutation in AC5 was found to produce only a small reduction in its inhibition by $G\alpha_i$ (less than 2-fold increase in IC50). A more significant effect on the binding of $G\alpha_i$ to AC1 may occur due to a difference in the C-terminal residue of the α3-helix of the C1 domain. In AC1, there is an alanine in this position, while in ACs 5 and 6, it is a valine. The wild-type AC5 construct used in [21] differed from the canonical sequence by having a methionine in this position (476 by their sequence numbering, 555 in the Uniprot sequence). They showed that mutating this residue to match the canonical sequence reduced the IC50 of $G\alpha_i$ by a third, while mutation to alanine gave a greater than 30-fold increase in IC50. Due to this apparent reduction in the affinity of AC1 for $G\alpha_i$, further MD simulations may be required to confirm the stability of a $G\alpha_{olf} \cdot AC1 \cdot G\alpha_i$ ternary complex. The lower sequence similarity between the C1 domains of ACs 1 and 5 also suggests that the allosteric effects on both the $G\alpha_{olf}/G\alpha_s$ binding groove and the active site could be different in a putative AC1 ternary complex. Again further MD simulations would be required to investigate this, as well as to further unravel the different computational properties of the AC isoforms found in different synapses.

Assumptions and limitations

As for any simulation study aimed at investigating *in vivo* subcellular processes, there are limitations that should be discussed. First, adenylyl cyclases, together with other components of the signal transduction networks they participate in, are organized as parts of multiprotein signaling complexes and/or are localized in structured microdomains in the cell which serve to compartmentalize the effects of the produced cAMP and efficiently activate downstream components of the networks and, ultimately, effectors [35–37, 39, 50]. The kinetic model here, on the other hand, assumes mass-action kinetics for the species included, i.e. it disregards any organization into multiprotein signaling complexes and instead describes a well-mixed solution of molecular species. This means that it reproduces the experimental measurements on cAMP in a partly phenomenological way. For example, AC5 needs to be presented with appropriate proportions of $G\alpha_{olf}$ and $G\alpha_i$ to reproduce the levels of cAMP, which may not necessarily be the same as the amounts of these proteins in real synapses. Second, a recent study has demonstrated that AC5 and the heterotrimeric G_{olf} protein are pre-assembled into a signaling complex and suggested that upon activation by the GPCR, the $G\alpha_{olf}$ subunit rearranges rather than physically dissociates from the Gβγ subunit [37]. This would imply an increase in the forward rate constant for AC5 and $G\alpha_{olf}$ binding predicted with the BD simulations. In light of this study, the effect of the hindered $G\alpha_{olf}$ binding to $AC5 \cdot G\alpha_i$ is not clear, since its main advantage of improving coincidence detection occurs precisely for values of k_{f1} around the BD estimates. It remains to be seen how much of an increase in the forward rate constant preassembly confers. A similar situation likely occurs for $G\alpha_i$, as well - the GPCRs and AC5 form oligomeric complexes that could include the G proteins [39], which would mean that the predicted value for the forward rate constant for AC5 and $G\alpha_i$ binding, k_{f2}, is also probably an underestimate. A larger value for k_{f2} is beneficial for coincidence detection both with the

simultaneous and the hindered simultaneous binding scheme (Fig 4G–4I). Finally, we should underline that the enzyme is additionally regulated by protein kinase A (PKA), calcium ions, nitric oxide, and the Gβγ subunit, and regulation via the transmembrane domains has been proposed (but not demonstrated so far) [4, 35, 51]. PKA is activated by cAMP and is the most common kinase to elicit the various downstream responses of the signal transduction network. PKA also inhibits AC5 via phosphorylation, and this is probably feedback that serves for signal termination. Calcium also inhibits AC5, an interaction which, due to excitatory synaptic input, might also help terminate its activity. The Gβγ enhances the effect of $G\alpha_s$ on AC5, but has no effect alone, and nitric oxide has an inhibitory effect whose purpose is also unknown. The measures for coincidence detection used here do not include these additional regulatory interactions, and this would provide a more complete picture of the enzyme's regulation in studies of various signaling scenarios.

On the same topic of molecular organization, while it is known that the D_2 and A_{2a} receptors are colocalized and form oligomeric complexes in D_2 MSNs, the same has not been demonstrated for the D_1 and M_4 receptors in D_1 MSNs. However, the D_1 and M_4 receptors have individually been reported in the postsynaptic density in striatal tissue (among other compartments) by electron microscopy [52,53], and activation of the M_4 receptors counteracts activation of the D_1 receptors both in striatal slices, as described above, and in striatal membrane preparations [17]. This makes it likely that they indeed colocalize enough to enable both G proteins to interact with AC5.

Furthermore, concerning the structural simulations carried out in the present study, it is appropriate to highlight some aspects. First, while the *apo* and the *holo* ternary complexes are relatively stable over about 2.1 and 1.1 μs of MD simulation time, respectively, we cannot exclude that on a longer time scale such complexes could show a dissociation of the different protein units. In this regard, it is worth mentioning that both simulations of the *apo* and *holo* forms of the ternary complex have been repeated starting with new velocities for about 0.6 and 1.0 μs, respectively, leading to the same overall conclusions described above. Second, in the systems simulated here, only the catalytic domains of AC5 are considered, while the transmembrane domains are not included. Although the transmembrane domains are important for the proper dimerization of the catalytic domains [54], the functionality of AC5 was experimentally found to be maintained upon removal of the transmembrane domains [21, 55]. It should also be noted that the structure of the AC5 catalytic domain modelled in this study does not include the C1b domain (whose structure has not yet been determined). The absence of this domain has been shown to reduce the sensitivity of AC5 to $G\alpha_i$ [21]. Nevertheless, the MD simulations performed here and by Van Keulen and Röthlisberger [24] show that $G\alpha_i$ is able to inhibit the activity of AC5 in the absence of the C1b domain. This suggests that the lower inhibition is due to the reduced affinity of $G\alpha_i$ in the absence of C1b, rather than to a change in the internal mechanism of inhibition. Were it possible to include C1b in the BD simulations, this might lead to an increase in the rate of $G\alpha_i$ association, which would lead to increased synergy in both the simultaneous and hindered binding schemes.

As mentioned above, the membrane-anchoring is also neglected in the BD simulations in which freely diffusing solutes are assumed. This assumption has two main effects on the predicted association rate constants, which alter the predictions in opposite directions, leading to some degree of cancellation of errors. The anchoring of AC5 and $G\alpha_{olf}$ in the membrane would add additional diffusional constraints that would potentially increase rates in vivo, by reducing the search space, while the slower diffusion of the lipid anchor in the membrane would slow down association.

It should also be noted that the simulated systems in this work were built by homology modelling using the then available X-ray crystal structures of AC as described in the Methods

section and also reported in previous studies [24, 56]. While this paper was in review, structures of AC9 including its two six-helix transmembrane domains (but not the C1b domain) were reported [57]. In order to check possible overlaps between atoms of the $G\alpha_i$ protein in our modelled ternary complex and atoms of the new AC9 structure (and of the membrane bilayer), we fitted the Cα atoms of the C1a and C2a domains on the respective atoms of the AC9 protein (see S15 Fig). The figure clearly shows that the position of the $G\alpha_i$ protein in the ternary complex does not overlap with the membrane. Moreover, the conformation, orientation and binding mode of the $G\alpha_i$ to AC5 would also be perfectly suitable for AC9 complexation, providing additional support for our model. Finally, although not all parts of the AC9 enzyme could be resolved, this new cryo-EM structure could provide a basis for future modelling work to investigate the effects of membrane tethering on AC5 regulation.

Conclusions

In this work, we have investigated the stability and activity of a $G\alpha_{olf} \cdot AC5 \cdot G\alpha_i$ ternary complex by MD simulation and found that the complex appears to be stable on the microsecond time scale, but is unable to catalyze ATP conversion. Using BD simulations, we have made predictions of the association rate constants for the formation of both binary AC5 · Gα complexes, and the subsequent association of the second Gα subunit to form the ternary complex.

Kinetic modelling of the AC5 signal transduction network showed that the predictions of the structure-based simulations maximize the ability of the network to recognize coincident neuromodulatory signals, with coincidence detection enhanced by both the presence of the ternary complex, and its reduced activity. Taken together, these results provide evidence that AC5 has evolved to perform coincidence detection of transient changes in the amounts of $G\alpha_{olf}$ and $G\alpha_i$ proteins, such that a brief deactivation of the $G\alpha_i$ signaling branch is needed to gate the $G\alpha_{olf}$ signal through. For the corticostriatal synapse on D_1 MSNs, this implies that both the transient rise in dopamine and the decrease in acetylcholine levels are necessary to trigger synaptic plasticity.

Methods

Modelling of binary AC5 complexes

The crystal structure (PDB ID 1AZS) of the ATP-free AC · $G\alpha_s$ complex [20] was used as a template for the catalytic region of AC5 and $G\alpha_{olf}$ in the *apo* ternary complex. The template used for the initial complex conformation included 1AZS's C1 and C2 domains (more specifically, canine AC5 for C1 and rat AC2 for C2) for modelling the AC5 structure (UniprotKB Q04400) from *Rattus norvegicus* as well as the $G\alpha_s$' structure for the initial $G\alpha_{olf}$ (UniprotKB P38406) conformation from *Rattus norvegicus* [20, 58, 59]. The modelled structure of the myristoylated *Rattus norvegicus* $G\alpha_i$ subunit (UniprotKB P10824) interacting with guanosine-5'-triphosphate (GTP) and Mg^{2+} was taken from [56]. $G\alpha_i$ also has several isoforms, and the one referred to here is $G\alpha_{i1}$. Myristoylation is a post-translational modification of the N-terminus of $G\alpha_i$ that results in the covalent attachment of a 14-carbon saturated fatty acid to the N-terminal glycine residue of $G\alpha_i$ via an amide bond. The modelled AC5 and $G\alpha_i$ structures were used for docking $G\alpha_i$ on AC5's C1 domain to finalise the initial conformation of the ternary complex. This *apo* ternary complex setup was also used to simulate the *apo* forms of AC5 · $G\alpha_i$ and AC5 · $G\alpha_{olf}$ by removing the subunit not to be considered.

The crystal structure (PDB ID 1CJK) of the catalytic AC domains with a bound ATP analogue (Adenosine-5'-rp-alpha-thio-triphosphate), ATPαS, and a $G\alpha_s$ interacting with the AC protein, was used as a template for the *holo* ternary complex. The template used for modelling

the active AC5 (UniprotKB Q04400) conformation in the ternary complex included the C1 and C2 domains from the PDB file 1CJK [22, 58, 59]. The $G\alpha_s$ subunit present in 1CJK was used as a template for the initial $G\alpha_{olf}$ (P38406) structure from *Rattus norvegicus* [22, 58, 59]. The modelled structure of the myristoylated *Rattus norvegicus* $G\alpha_i$ subunit (UniprotKB P10824) interacting with GTP and Mg^{2+} was taken from [56]. The active myristoylated *Rattus norvegicus* $G\alpha_i$ is referred to simply as $G\alpha_i$ because only a myristoylated form of $G\alpha_i$ was used in all simulations.

Modelling of ternary AC5 complexes

Membrane-bound ACs consist of two membrane-bound regions and two cytosolic domains. The latter form the active site of the enzyme and its structure has been determined by crystallography. The catalytic domains, C1 and C2, are located close to the membrane due to AC5's transmembrane domains, but remain entirely solvated. The crystal structure templates, used for modelling the complexes, were employed to determine the orientation of $G\alpha_{olf}$ on the C2 domain. The HADDOCK web server [60] was used for docking ten conformations of the active $G\alpha_i$ subunit to AC5's catalytic domains in the *apo* and *holo* forms as described in [24]. The active region of $G\alpha_i$ was defined in HADDOCK as a large part of the alpha helical domain (112-167), the switch I region (175-189) and the switch II region (200-220), allowing for a large unbiased area on the $G\alpha_i$ protein surface to be taken into account during docking. The active region of AC5's C1 domain was defined as the α1 helix (479-490) and the C-terminal region of the α3 helix (554-561) because experimentally it has been found that $G\alpha_i$ is unable to interact with C2 and its main interactions with AC5 are with the C1 domain [21]. Ten snapshots of $G\alpha_i$ were used for docking the Gα subunit to the catalytic domain of AC5. These snapshots were extracted at time intervals of 0.5 ns from the end of the classical MD trajectory of $G\alpha_i$ (around 1.9 μs) described in [56]. The same three criteria for complex selection as in [24] were applied: (1) the absence of overlap between the C2 domain and $G\alpha_i$, (2) no overlap with the GTP binding region of $G\alpha_i$ and the C1 domain of AC5, and (3) presence of similar complexes in the top-ten docking results of the docking calculations performed for all ten used $G\alpha_i$ conformations.

Classical molecular dynamics simulations

The Gromacs 5.1.2 software [61, 62] was used to perform the simulations. The *apo* and *holo* $G\alpha_{olf} \cdot AC5 \cdot G\alpha_i$ systems, which were simulated for 2.1 μs and 1.2 μs respectively, each include two GTP molecules. In addition, the *holo* complex incorporates four Mg^{2+} ions and one ATP molecule, while in the *apo* form only three Mg^{2+} ions are present. Both *apo* and the *holo* systems were solvated in about 162,000 water molecules and 150 mM KCl. They were simulated at a temperature of 310 K and a pressure of 1 bar, maintained using the Nosé-Hoover thermostat and an isotropic Parrinello-Rahman barostat, respectively. The force fields used for the protein and the water molecules were AMBER99SB [63] and TIP3P [64]. For GTP and ATP, the force field generated by Meagher et al. was used [65]. The adjusted force field parameters for Cl^- and K^+ were taken from [66]. The Mg^{2+} parameters originated from [67] and the parameter set for the myristoyl group was taken from [56]. Electrostatic interactions were calculated with the Ewald particle mesh method with a real space cutoff of 12Å. The van der Waals interactions also had a cutoff of 12 Å. Bonds involving hydrogen atoms were constrained using the LINCS algorithm [68] The integration time step was set to 2 fs.

The *apo* binary complexes, $AC5 \cdot G\alpha_i$ and $AC5 \cdot G\alpha_{olf}$, used for comparison to the ternary complexes, were built via the same procedure and were each simulated for 3 μs.

The first step in the equilibration procedure of the protein systems included the energy minimisation of the protein complex together with the ligands (Mg^{2+}, GTP, ATP), referred to as the complete complex. Position restraints of 1000 kJ mol^{-1} nm^{-2} were applied to the structure of the complete complex during energy minimisation. The next step that was performed was the simulation of the complete complex under canonical NVT (constant number of atoms (N), constant volume (V) and constant temperature (T)) conditions, starting from the energy minimised structure, with position restraints of 1000 kJ mol^{-1} nm^{-2} on the complete complex. The length of the NVT run was 2 ns. The third step included the performance of a 4 ns isothermal-isobaric NPT run (constant number of atoms (N), constant pressure (P) and constant temperature (T)) with position restraints of 1000 kJ mol^{-1} nm^{-2} on the complete complex. The fourth step was an NPT simulation of 4 ns, with position restraints of 1000 kJ mol^{-1} nm^{-2} on the complete complex except for the hydrogens of the proteins. The fifth step contained an NPT run of 4 ns in which the backbone of the proteins were restrained by 1000 kJ mol^{-1} nm^{-2} as well as the ligands. The sixth step was an unrestrained NPT simulation of at least 10 ns, which was prolonged depending on the RMSD convergence of the proteins in the equilibrated system.

Forward rate constant estimation via Brownian dynamics simulations

Brownian dynamics (BD) simulations were performed to estimate the forward association rate constants in the two schemes in Fig 3. The simulations were performed using the SDA 7 software package [69], with the associating species represented in atomic resolution as rigid bodies. The inter-species interactions were modeled using the effective charge model [70], with the electrostatic desolvation term described by Elcock et al. [71], and following the parameterization of Gabdoulline and Wade [72].

The atomic structures of the reactant species in the forward reactions shown in Fig 3B and 3C were taken from clustered snapshots of the MD simulations described above, except for the structures of *apo* AC5 and $G\alpha_i$ used to calculate k_{f2}, which were obtained from simulations performed by Van Keulen and Röthlisberger [24]. The electrostatic potential of each snapshot of the reactant species was calculated via solution of the linearized Poisson-Boltzmann equation (PBE) using the APBS PBE solver [73], such that at the grid boundaries, the electrostatic potentials matched those of atom-centered Debye-Hückel spheres. The atomic charges of the protein residues were taken from the Amber force field, with the charges of the myristoyl moiety as described in [56] and the GTP charges as described by Meagher et al. [65]. The low-dielectric cavity ($\varepsilon_r = 4$) was described using Bondi atomic radii [74] and the smoothed molecular surface definition of Bruccoleri et al. [75], while the solvent was modelled using a dielectric constant of 78, and a 150 mM concentration of salt with monovalent ions of radius 1.5 Å. For the single species reactants, solution of the linearized PBE generated cubic potential grids with 129 grid points per dimension, spaced at 1 Å, while larger grids with 161 points per dimension were generated for the binary reactants. Effective charges were calculated using the *ECM* module of SDA 7 [69, 70], with charge sites placed on the heteroatoms of ionized amino acid side chains and termini, the phosphate oxygen and phosphorus atoms of ATP and GTP, and Mg^{2+} ions. The effective charges of each solute were fitted such that, in a homogeneous dielectric environment, they reproduced the solute's electrostatic potential computed by solving the PBE in a skin bound by the surfaces described by rolling probe spheres of radii 4 and 7 Å along the molecular surface of the solute. Electrostatic desolvation potentials were calculated using the *make_edhdlj_grid* tool in SDA 7 [69].

For each reaction, four BD simulations of 50 000 trajectories were performed using each MD snapshot, and rate constants were calculated using the Northrup, Allison and

McCammon formalism [76]. The mean and standard deviations across these four simulations was then determined. The average value for the corresponding rate constant was computed across all MD snapshots. The infinite dilution diffusion coefficients of each reaction species were calculated using HYDROPRO [77, 78] with the exception of those of the AC5 · Gα complex reactants in the ternary complex forming reactions, for which the diffusion coefficients of AC5 were used. In each simulation trajectory, the position of the center of AC5, or the reactant complex, was fixed at the center of the simulated volume, while the initial position of the center of the reactant Gα subunit was placed on the surface of a sphere of radius b, centered on the other reactant, with b taken as equal to the sum of the maximal extent of the distance of an atom of either reactant from the reactant center, plus the maximal extent of any interaction grid point to the solute center plus 30 Å. The simulations continued until the reactants diffused to a separation c, where $c = 3b$. Trajectories were assumed to have formed reactive encounter complexes when two independent native contacts between the two reactants reach a separation of 6.5 Å or less. Native contacts were defined as a pair of hydrogen bonding heteroatoms, separated by less than 5 Å in the bound complex. Two native contacts were assumed to be independent if the heteroatoms on the same solute that form the contacts were separated by more than 6 Å. This definition of an encounter complex has been shown to result in calculated protein-protein association rate constants that correlate well with experimental values [72].

Kinetic model of the signal transduction network

The kinetic model of the signal transduction network is a system of coupled ordinary differential equations with mass-action kinetics modeling the network's biochemical reactions. For example, for the reaction $A + B \underset{k_r}{\overset{k_f}{\leftrightarrows}} C$, the rate at which it occurs is given with:

$$v = \frac{d[C]}{dt} = -\frac{d[A]}{dt} = -\frac{d[B]}{dt} = k_f[A][B] - k_r[C]$$

In order to reduce the number of rate constants that would need estimation, our aim was to use a minimal model with which we could still study the coincidence detection ability of the enzyme and capitalize on the predictions of the molecular simulations. We have used two versions of the model, one with the allosteric exclusion and the other with the simultaneous binding scheme for AC5 regulation in Fig 3. The full reaction networks are given in S8 Fig. The two versions of the model have 8 and 16 rate constants, respectively. In Fig 3, we have additionally used versions of the model which included cAMP production to illustrate the correspondence between k_c and the levels of cAMP and thus rationalize the use of k_c as a proxy for the cAMP levels. The reactions and parameters for cAMP production and degradation have been taken from [15].

There are no receptors included in the model, and the Da↑ and ACh↓ inputs are modeled as changes in the rate constants for the conversion of inactive to active G proteins. Pools of inactive G_{olf} and G_i are activated at rates of $k_{fG_{olf}} = 5s^{-1}$ and $k_{fG_i} = 5s^{-1}$ when Da or ACh is present. This eliminates the parameters that would have corresponded to the reactions of ligand and receptor binding, and G protein and receptor binding. Additionally, we have omitted the heterotrimeric nature of the G proteins, i.e. we have not included the Gβγ subunit in the model. The G proteins are modeled as simply switching between an active and inactive form. The value for the rate of $G\alpha_i$ activation is chosen so that there is a high resting-level inhibition of AC5 by the tonic level of ACh, which is a plausible assumption based on recent experimental results [14]. The value for k_{fGolf} is, similarly, chosen to achieve amounts of active G_{olf} high enough to drive the binding reactions with AC5 and AC5 · $G\alpha_i$ forward. The total

amounts of AC5 and the two G proteins used for this model are n_{AC5} = 1500 nM, n_{Golf} = 1500 nM and n_{Gi} = 6000 nM.

The activated $G\alpha_{olf}$ and $G\alpha_i$ interact with AC5 and can form each of the binary complexes and the ternary complex. Their deactivation is done by the intrinsic GTPase activity of the G proteins themselves, but is increased by AC5 for the case of $G\alpha_s$ (a homologue to $G\alpha_{olf}$) at least fivefold and the regulator of G protein signaling 9-2 (RGS9-2) for $G\alpha_i$ 20 to 40 times [41, 79], for which reason we have used values of $k_{rG_{olf}} = 0.5s^{-1}$ and $k_{rG_i} = 5s^{-1}$. If deactivated, the G proteins unbind from AC5. For the reverse (unbinding) rates of the G proteins from the binary AC5 complexes, we use values 100 times greater than the corresponding forward rate constants, which is the order of magnitude fitted in [23]. The reverse rates of G protein unbinding from the ternary complex, are increased by an order of magnitude compared to the reverse rates for unbinding from the respective binary complexes to qualitatively incorporate possible reduced stability of the ternary complex compared to the binary complexes on longer time scales (see Results section).

The remaining parameters, the forward rate constants of the G proteins' binding to AC5 and the binary complexes AC5 · $G\alpha_{olf}$ and AC5 · $G\alpha_i$, were estimated with the BD simulations (see Table 1). We have also varied these to explore their effects on the network's ability to perform coincidence detection.

Measures of coincidence detection

As was defined in the introduction, for the signal transduction network that we consider, coincidence detection means to respond with significant amounts of cAMP only when the two incoming signals Da ↑ and ACh ↓ coincide in time and in the spatial vicinity of the receptors. Note that there are two aspects of coincidence detection in the definition:

a. distinguishing between the inputs Da ↑ + ACh ↓, and a Da ↑ or ACh ↓ alone, and

b. responding strongly enough with amounts of cAMP that are physiologically relevant.

To quantify how well the network distinguishes between the different inputs, we use the synergy quantity, and to quantify the strength of the response, we use the average catalytic rate, both defined below.

Average catalytic rate. The average catalytic rate is an average of the catalytic rates of the unbound form of AC5 and each of the complexes with the Gα subunits. For the allosteric exclusion scheme in Fig 3B, where the ternary complex does not form, it is:

$$k_c = p_1 k_{c,AC5} + p_2 k_{c,AC5\cdot G\alpha_{olf}} + p_3 k_{c,AC5\cdot G\alpha_i}$$

with the weights

$$p_1 = \frac{[AC5]}{[AC5] + [AC5 \cdot G\alpha_{olf}] + [AC5 \cdot G\alpha_i]},$$

$$p_2 = \frac{[AC5 \cdot G\alpha_{olf}]}{[AC5] + [AC5 \cdot G\alpha_{olf}] + [AC5 \cdot G\alpha_i]},$$

$$p_3 = \frac{[AC5 \cdot G\alpha_i]}{[AC5] + [AC5 \cdot G\alpha_{olf}] + [AC5 \cdot G\alpha_i]}.$$

being the amounts of each enzyme species in the allosteric exclusion scheme as a fraction of

the total concentration of AC5 in the system. For the simultaneous binding scheme where the ternary complex does form, the average catalytic rate is

$$k_c = q_1 k_{c,AC5} + q_2 k_{c,AC5\cdot G\alpha_{olf}} + q_3 k_{c,AC5\cdot G\alpha_i} + q_4 k_{c,G\alpha_{olf}\cdot AC5\cdot G\alpha_i}$$

with

$$q_1 = \frac{[AC5]}{[AC5] + [AC5\cdot G\alpha_{olf}] + [AC5\cdot G\alpha_i] + [G\alpha_{olf}\cdot AC5\cdot G\alpha_i]},$$

$$q_2 = \frac{[AC5\cdot G\alpha_{olf}]}{[AC5] + [AC5\cdot G\alpha_{olf}] + [AC5\cdot G\alpha_i] + [G\alpha_{olf}\cdot AC5\cdot G\alpha_i]},$$

$$q_3 = \frac{[AC5\cdot G\alpha_i]}{[AC5] + [AC5\cdot G\alpha_{olf}] + [AC5\cdot G\alpha_i] + [G\alpha_{olf}\cdot AC5\cdot G\alpha_i]},$$

$$q_4 = \frac{[G\alpha_{olf}\cdot AC5\cdot G\alpha_i]}{[AC5] + [AC5\cdot G\alpha_{olf}] + [AC5\cdot G\alpha_i] + [G\alpha_{olf}\cdot AC5\cdot G\alpha_i]}.$$

We assume that the catalytic rate of the unbound AC5 is $k_{c,AC5} = 0.1s^{-1}$, and this rate is scaled by factors of $\alpha_{G\alpha_{olf}}$ and $\alpha_{G\alpha_i}$ when the respective regulator G protein subunit binds:

$$k_{c,AC5\cdot G\alpha_{olf}} = \alpha_{G\alpha_{olf}} k_{c,AC5}$$

$$k_{c,AC5\cdot G\alpha_i} = \alpha_{G\alpha_i} k_{c,AC5}$$

The factors of stimulation and inhibition of AC5 are set to be $\alpha_{G\alpha_{olf}} = 200$ ([23]) and $\alpha_{G\alpha_i} = 0.01s^{-1}$. For the catalytic rate of the ternary complex, we use the result of the MD simulations that the ternary complex is inactive, $\alpha_{G\alpha_{olf},G\alpha_i} = \alpha_{G\alpha_i}$, i.e.:

$$k_{c,G\alpha_{olf}\cdot AC5\cdot G\alpha_{olf}} = \alpha_{G\alpha_i} k_{c,AC5},$$

except in Fig 3D, 3E and 3F, where the catalytic rate of the ternary complex is varied to investigate its effect on coincidence detection.

Synergy. The synergy of two signals s_1 and s_2 is defined as

$$S(t) = \frac{r(s_1, s_2, t)}{r(s_1, t) + r(s_2, t) - r_{ss}},$$

where r_{ss} is the response at steady state. This quantity measures how strong the response r of the signal transduction network is for two coincident signals compared to the responses for single signals. The synergistic effect of the input signals can be examined in light of any quantity of interest in the network that is affected by the inputs, such as the level of activated PKA, for example [15]. Not having included PKA or cAMP in the kinetic model, we use the average catalytic rate k_c as a proxy for the amount of cAMP produced, since the latter directly depends on k_c. That is, the synergy of a simultaneous Da ↑ and ACh ↓ is:

$$S(t) = \frac{k_c(Da\uparrow, ACh\downarrow, t)}{k_c(Da\uparrow, t) + k_c(ACh\downarrow, t) - k_{c,ss}}.$$

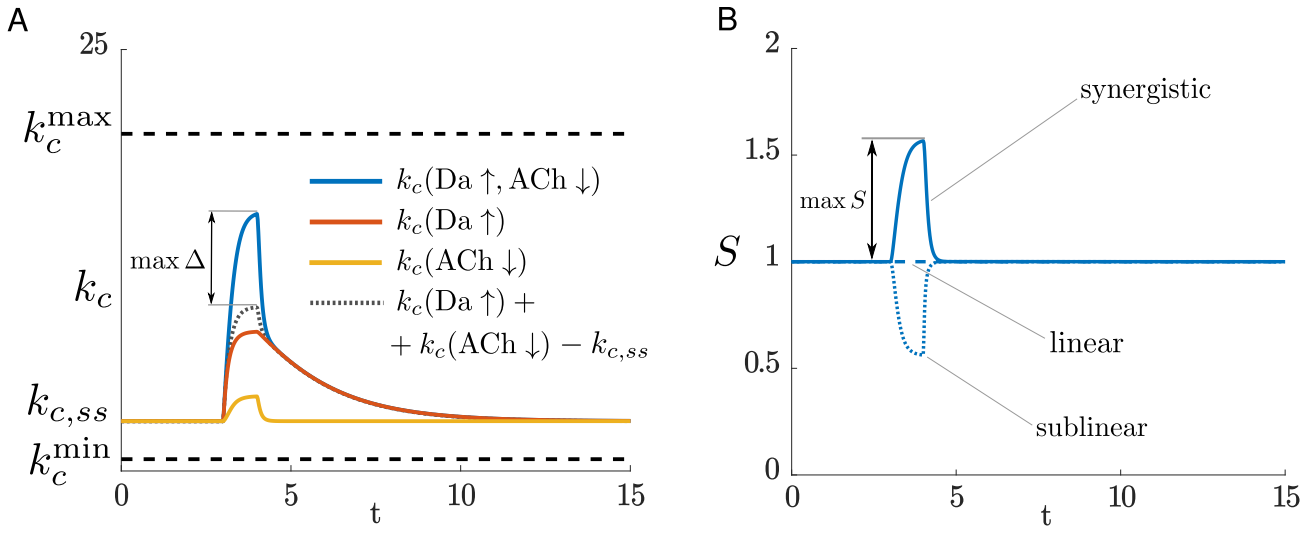

Fig 6. **A** A cartoon of the average catalytic rate during each of the input situations Da ↑ + ACh ↓, Da ↑, and ACh ↓. **B** The synergy corresponding to panel (A). In addition, the dashed and dotted lines illustrate how the synergy for a linear and a sublinear response would look like, respectively.

https://doi.org/10.1371/journal.pcbi.1007382.g006

S(t) > 1 indicates a nonlinearly greater response in the presence of the two coincident signals, S(t) = 1 indicates a linear response to the coincident signals, and S(t) < 1 is a sublinear response. Hence, the case S(t) > 1 indicates that the signal transduction network can perform coincidence detection, whereas S(t) ≤ 1 indicates an inability to do so.

Example traces for k_c and the corresponding synergy are given in Fig 6.

Using

$$\Delta = k_c(Da\uparrow, ACh\downarrow, t) - (k_c(Da\uparrow, t) + k_c(ACh\downarrow, t) - k_{c,ss})$$

to express the difference between the response of the network for two coincident signals and the response for single signals, the expression for the synergy can also be rewritten as

$$S(t) = \frac{k_c(Da\uparrow, ACh\downarrow, t)}{k_c(Da\uparrow, t) + k_c(ACh\downarrow, t) - k_{c,ss}} = 1 + \frac{\Delta}{k_c(Da\uparrow, t) + k_c(ACh\downarrow, t) - k_{c,ss}}.$$

The difference in the responses, Δ, determines how big the synergistic effect of the input signals is (Fig 6).

Fig 6 is an example depicting how k_c relates to the synergy. There are minimum and maximum bounds on k_c: it would attain the minimum value k_c^{min} if all of AC5 were inhibited by $G\alpha_i$, that is, only the catalytically inactive complex AC5 · $G\alpha_i$ exists, where k_c^{min} is the catalytic rate of AC5 · $G\alpha_i$ (see above). Analogously, it would attain the maximum value k_c^{max} if all of AC5 were bound in the catalytically active complex AC5 · $G\alpha_{olf}$, where k_c^{max} is its catalytic rate (see above). In the models we use in this study, AC5 is never fully occupied by either of the Gα subunits, and hence k_c is always between the minimum and maximum bounds. To maximize Δ, one would need to have k_c grow towards the maximum as much as possible during Da↑ + ACh↓, and to have it as low as possible at steady state, and when each of the signals Da↑ and ACh↓ comes alone.

The metric C combines S and k_c. A combination of the average catalytic rate and the synergy gives a metric which can be helpful to evaluate whether the network both distinguishes between the different input situations and responds strongly. We use a product of k_c and S for this purpose, $C = Sk_c$.

Supporting information

S1 Fig. Root-mean-square deviations of three apo complexes: $G\alpha_{olf}$ · AC5 · $G\alpha_{i1}$, AC5 · $G\alpha_{i1}$ and AC5 · $G\alpha_{olf}$. (Top panel) Individual RMSD values for C1, C2, $G\alpha_{i1}$ and $G\alpha_{olf}$ in the ternary complex only including the backbone of the domains. In the case of $G\alpha_{i1}$, residues 33 to 345 were taken into account during the RMSD calculation as the C and N termini are not structured. (Middle panel) Individual RMSD values for C1, C2 and $G\alpha_{i1}$ in the binary AC5 · $G\alpha_{i1}$ complex only including the backbone of the domains. In the case of $G\alpha_{i1}$, residues 33 to 345 were taken into account during the RMSD calculation as the C and N termini are not structured. (Bottom panel) Individual RMSD values for C1, C2 and $G\alpha_{olf}$ in the binary AC5 · $G\alpha_{olf}$ complex only including the backbone of the domains.
(EPS)

S2 Fig. Time evolution of the secondary structures for AC5 (top), $G\alpha_i$ (middle), and $G\alpha_{olf}$ (bottom) along the trajectory of the *apo* ternary complex.
(EPS)

S3 Fig. Time evolution of the secondary structures for AC5 (top), and $G\alpha_i$ (bottom), along the trajectory of the *apo* binary complex AC5 · $G\alpha_i$.
(EPS)

S4 Fig. Time evolution of the secondary structures for AC5 (top), and $G\alpha_{olf}$ (bottom), along the trajectory of the *apo* binary complex AC5 · $G\alpha_{olf}$.
(EPS)

S5 Fig. Time evolution of the number of hydrogen bonds present in the three simulated *apo* complexes along the respective MD trajectories.
(EPS)

S6 Fig. Root-mean-square fluctuations per residue calculated on the protein backbone of the different subunits (from top to bottom, AC5:C1, AC5:C2, $G\alpha_i$, and $G\alpha_{olf}$) of the three simulated *apo* complexes.
(EPS)

S7 Fig. Radius of gyration calculated along the MD trajectories of the three simulated apo complexes, $G\alpha_{olf}$ · AC5 · $G\alpha_i$, AC5 · $G\alpha_i$, and AC5 · $G\alpha_{olf}$. The dashed lines indicate the values of the radius of gyration in the initial structures.
(EPS)

S8 Fig. The full kinetic models of the signal transduction networks used in this study.
(EPS)

S9 Fig. The effect of the interaction motif between AC5 and the regulatory Gα subunits on coincidence detection. For the allosteric exclusion and simultaneous binding schemes, respectively, the amounts of each enzyme species as a percentage of the total amount of AC5 are shown for the cases of Da ↑ + ACh ↓ (A,F), Da ↑ (B, G), and ACh ↓ (C, H). (D, I) Average catalytic rate for each scheme. (E, J) cAMP levels for each scheme.
(EPS)

S10 Fig. Time window for coincidence detection. (A) The detection window for the allosteric exclusion scheme and simultaneous binding scheme. Arrows are the time differences between ACh ↓ and Da ↑ chosen for the traces below. (B) The percentage of each AC5 species as a fraction of the total amount of AC5, (C) average catalytic rate, (D) synergy for the allosteric exclusion scheme. (E), (F), and (G) are the same quantities for the simultaneous binding scheme.

Note the shared axes.
(EPS)

S11 Fig. (A) The maximum of the synergy, (B) the maximum of kc, (C) the maximum of the metric C as dependent on the rate of Gαi deactivation, krGi.
(EPS)

S12 Fig. Behavior of the two signal transduction schemes for different values of the association rate constants. From left to right: the percentage of enzyme species for Da ↑ + ACh ↓, the percentage of enzyme species for Da ↑, the average catalytic rate, and the synergy, for the simultaneous binding scheme for (A) $k_{f1} = k_{f4} = 0.002$ $(nMs)^{-1}$, $k_{f2} = k_{f3} = 2$ $(nMs)^{-1}$, and (B) $k_{f1} = k_{f4} = 2$ $(nMs)^{-1}$, $k_{f2} = k_{f3} = 2$ $(nMs)^{-1}$ and the hindered simultaneous binding scheme for (C) $k_{f1} = k_{f4} = 0.002$ $(nMs)^{-1}$, $k_{f2} = k_{f3} = 2$ $(nMs)^{-1}$ and (D) $k_{f1} = k_{f4} = 2$ $(nMs)^{-1}$, $k_{f2} = k_{f3} = 2$ $(nMs)^{-1}$. Note the shared axes.
(EPS)

S13 Fig. Structure of $G\alpha_{olf}$ in the modelled AC5 · $G\alpha_{olf}$ complex and sequence alignment of $G\alpha_{olf}$ and $G\alpha_s$. The structure of $G\alpha_{olf}$ in the modelled AC5 · $G\alpha_{olf}$ *apo* complex (A). The highlighted regions show the switch II helix residues that interact the C2 binding groove on AC5 (magenta) and other amino acid residues that are within 6 of AC5 in the modelled structure. The sequence alignment of rat $G\alpha_{olf}$ (GNAL) and $G\alpha_s$ (GNAS2) (B). The magenta and green regions show the residues highlighted in (A). The yellow region shows the N-terminal residues not included in the structure used in this work.
(EPS)

S14 Fig. Multiple sequence alignment for all mouse AC isoforms with the colors matching those the structure in Fig 5A. The sequences were taken from Uniprot, and aligned using Clustal Omega within Uniprot. The red and blue boxes show positions where AC1 has substitutions compared to AC5, as described in Fig 5.
(EPS)

S15 Fig. Initial modelled configuration of the $G\alpha_{olf}$ · AC5 · $G\alpha_i$ ternary complex used in our classical MD simulations, after fitting of Cα atoms of C1a and C2a domains on the respective Cα atoms of the AC9 protein (PDB ID: 6R3Q). AC9 (pale yellow) consisting of the transmembrane domain (TM), the helical domain (HD), and the two pseudo-symmetric C1a and C2a domains, is fully shown in cartoon representation. The two domains C1a (blue) and C2a (red) of AC5 in complex with $G\alpha_i$ (cyan) and $G\alpha_{olf}$ (gray) proteins are also represented as a cartoon.
(EPS)

S16 Fig. The allosteric exclusion scheme does not support coincidence detection for saturating concentrations of $G\alpha_{olf}$.
(EPS)

S1 Table. Bimolecular association rate constants $(nMs)^{-1}$ for the forward reactions computed via BD simulations. Each rate constant was calculated using a number of snapshots from MD simulations. The reported numbers for each snapshot are the mean values estimated from 4 BD simulations of 50 000 trajectories (standard deviation in parentheses). Rate constants were calculated for complexes including apo and holo AC5 (superscripts a and h respectively).
(XLSX)

S1 Text. The allosteric exclusion scheme inherently lacks the ability for coincidence detection.
(PDF)

Acknowledgments

The authors thank Pietro Vidossich for scientific discussions during this project.

Author Contributions

Conceptualization: Ursula Röthlisberger, Rebecca C. Wade, Paolo Carloni, Jeanette Hellgren Kotaleski.

Funding acquisition: Ursula Röthlisberger, Rebecca C. Wade, Paolo Carloni, Jeanette Hellgren Kotaleski.

Investigation: Neil J. Bruce, Daniele Narzi, Daniel Trpevski, Siri C. van Keulen, Anu G. Nair, Ursula Röthlisberger, Rebecca C. Wade, Paolo Carloni, Jeanette Hellgren Kotaleski.

Methodology: Neil J. Bruce, Daniele Narzi, Daniel Trpevski, Siri C. van Keulen, Anu G. Nair, Ursula Röthlisberger, Rebecca C. Wade, Paolo Carloni, Jeanette Hellgren Kotaleski.

Project administration: Jeanette Hellgren Kotaleski.

Supervision: Ursula Röthlisberger, Rebecca C. Wade, Paolo Carloni, Jeanette Hellgren Kotaleski.

Writing – original draft: Neil J. Bruce, Daniele Narzi, Daniel Trpevski, Siri C. van Keulen, Anu G. Nair.

Writing – review & editing: Neil J. Bruce, Daniele Narzi, Daniel Trpevski, Siri C. van Keulen, Anu G. Nair, Ursula Röthlisberger, Rebecca C. Wade, Paolo Carloni, Jeanette Hellgren Kotaleski.

References

1. Glatt CE, & Snyder SH. (1993). Cloning and expression of an adenylyl cyclase localized to the corpus striatum. *Nature*, 361, 536–538. https://doi.org/10.1038/361536a0 PMID: 8429907
2. Mons M, & Cooper DMF. (1994). Selective expression of one Ca2+-inhibitable adenylyl cyclase in dopaminergically innervated rat brain regions. *Molecular Brain Research*, 22, 236–244. https://doi.org/10.1016/0169-328x(94)90052-3 PMID: 8015383
3. Changeux J-P. & Edelstein SJ. (2005). Allosteric mechanisms of Signal Transduction. *Science*, 308, 1424–1428. https://doi.org/10.1126/science.1108595 PMID: 15933191
4. Linder JU. (2006). Class III adenylyl cyclases: Molecular mechanisms of catalysis and regulation. *Cellular and Molecular Life Sciences*, 63(15), 1736–1751. https://doi.org/10.1007/s00018-006-6072-0 PMID: 16786220
5. Linder JU, & Schultz JE. (2003). The class III adenylyl cyclases: Multi-purpose signalling modules. *Cellular Signalling*, 15(12), 1081–1089. https://doi.org/10.1016/s0898-6568(03)00130-x PMID: 14575863
6. Sadana R, & Dessauer CW. (2009). Physiological roles for G protein-regulated adenylyl cyclase isoforms: insights from knockout and overexpression studies. *Neurosignals*, 17, 5–22. https://doi.org/10.1159/000166277 PMID: 18948702
7. Anholt RRH. (1994). Signal integration in the nervous system: adenylate cyclases as molecular coincidence detectors. *Trends in Neurosciences*, 17(1), 37–41. https://doi.org/10.1016/0166-2236(94)90033-7 PMID: 7511849
8. Bourne H. R., & Nicoll R. (1993). Molecular machines integrate coincident synaptic signals. *Cell*, 72 (1001), 65–75. https://doi.org/10.1016/S0092-8674(05)80029-7

9. Delmeire D, Flamez D, Hinke SA, Cali JJ, Pipeleers D, & Schuit F. (2003). Type VIII adenylyl cyclase in rat beta cells: Coincidence signal detector/generator for glucose and GLP-1. *Diabetologia*, 46(10), 1383–1393. https://doi.org/10.1007/s00125-003-1203-8 PMID: 13680124

10. Impey S, Wayman G, Wu Z, & Storm DR. (1994). Type I Adenylyl Cyclase Functions as a Coincidence Detector for Control of Cyclic AMP Response Element-Mediated Transcription: Synergistic Regulation of Transcription by Ca2+ and Isoproterenol. *Molecular and Cellular Biology*, 14(12), 8272–8281. https://doi.org/10.1128/mcb.14.12.8272 PMID: 7969163

11. Lustig KD, Conklin BR, Herzmark P, Taussig R, & Bourne HR. (1993). Type II adenylylcyclase integrates coincident signals from Gs, Gi, and Gq. *Journal of Biological Chemistry*, 268(19), 13900–13905. PMID: 8390980

12. McVey M, Hill J, Howlett A, & Klein C. (1999). Adenylyl cyclase, a coincidence detector for nitric oxide. *Journal of Biological Chemistry*, 274(27), 18887–18892. https://doi.org/10.1074/jbc.274.27.18887 PMID: 10383385

13. Mons N, Guillou JL, & Jaffard R. (1999). The role of Ca2+/calmodulin-stimulable adenylyl cyclases as molecular coincidence detectors in memory formation. *Cellular and Molecular Life Sciences*, 55(4), 525–533. https://doi.org/10.1007/s000180050311 PMID: 10357223

14. Nair AG, Castro LRV, Khoury M. El, & Vincent P. (2019). The high efficacy of muscarinic M4 receptor in D1 medium spiny neurons reverses striatal hyperdopaminergia. *Neuropharmacology*, 146, 74–83. https://doi.org/10.1016/j.neuropharm.2018.11.029 PMID: 30468798

15. Nair AG, Gutierrez-Arenas O, Eriksson O, Vincent P, & Hellgren Kotaleski J. (2015). Sensing Positive versus Negative Reward Signals through Adenylyl Cyclase-Coupled GPCRs in Direct and Indirect Pathway Striatal Medium Spiny Neurons. *Journal of Neuroscience*, 35(41), 14017–14030. https://doi.org/10.1523/JNEUROSCI.0730-15.2015 PMID: 26468202

16. Onali P, Olianas MC. (2002) Muscarinic M4 receptor inhibition of dopamine D1-like receptor signalling in rat nucleus accumbens. *European Journal of Pharmacology* 448(2–3): 105–111, https://doi.org/10.1016/s0014-2999(02)01910-6 PMID: 12144929

17. Jeon J, Dencker D, Wörtwein G, Woldbye DPD, Cui Y, Davis AA, Levey AI, Schütz G, Sager TN, Mørk A, Li C, Deng C-X, Fink-Jensen A and Wess J (2010). A Subpopulation of Neuronal M4 Muscarinic Acetylcholine Receptors Plays a Critical Role in Modulating Dopamine-Dependent Behaviors. *Journal of Neuroscience* 30 (6) 2396–2405, https://doi.org/10.1523/JNEUROSCI.3843-09.2010 PMID: 20147565

18. Ferre S, Quiroz C, Woods AS, Cunha R, Popoli P, Ciruela F, Lluis C, Franco R, Azdad K, and Schiffmann SN. (2008) An Update on Adenosine A2A-Dopamine D2 Receptor Interactions: Implications for the Function of G Protein-Coupled Receptors. *Current Pharmaceutical Design*, 14,(15) 1468–1474(7) https://doi.org/10.2174/138161208784480108 PMID: 18537670

19. Yapo C, Nair AG, Clement L, Castro LR, Hellgren Kotaleski J, & Vincent P. (2017). Detection of phasic dopamine by D1 and D2 striatal medium spiny neurons. *Journal of Physiology*, 595(24), 7451–7475. https://doi.org/10.1113/JP274475 PMID: 28782235

20. Tesmer JJ, Sunahara RK, Gilman AG, & Sprang SR. (1997) Crystal structure of the catalytic domains of adenylyl cyclase in a complex with Gsalpha.*GTPgammaS Science* 278:1907–1916. https://doi.org/10.1126/science.278.5345.1907 PMID: 9417641

21. Dessauer CW, Tesmer JJG, Sprang SR, & Gilman AG. (1998). Identification of a Gi Binding Site on Type V Adenylyl Cyclase. *Journal of Biological Chemistry*, 273(40), 25831–25839. https://doi.org/10.1074/jbc.273.40.25831 PMID: 9748257

22. Tesmer JJG, Sunahara RK, Johnson RA, Gosselin G, Gilman AG, & Sprang SR. (1999). Two-metal-Ion catalysis in adenylyl cyclase. *Science*, 285(5428), 756–760. https://doi.org/10.1126/science.285.5428.756 PMID: 10427002

23. Chen-Goodspeed M, Lukan AN, & Dessauer CW. (2005). Modeling of Gas and Gai regulation of human type V and VI adenylyl cyclase. *Journal of Biological Chemistry*, 280(3), 1808–1816. https://doi.org/10.1074/jbc.M409172200 PMID: 15545274

24. Van Keulen SC, & Rothlisberger U. (2017b). Exploring the Inhibition Mechanism of Adenylyl Cyclase Type 5 by N-terminal Myristoylated Gαi1:GTP. *PLoS Computational Biology*, 13(9), e1005673. https://doi.org/10.1371/journal.pcbi.1005673 PMID: 28892485

25. Frezza E, Martin J, & Lavery R. (2018) A molecular dynamics study of adenylyl cyclase: The impact of ATP and G-protein binding. PLoS ONE 13(4): e0196207. https://doi.org/10.1371/journal.pone.0196207

26. Hollingsworth S, and Dror RO. (2018). Molecular Dynamics Simulation for All. *Neuron* 99(6): 1129–1143. https://doi.org/10.1016/j.neuron.2018.08.011 PMID: 30236283

27. Stein M, Gabdoulline RR, Wade RC. (2007). Bridging from molecular simulation to biochemical networks. *Current Opinion in Structural Biology*, 17(2), 166–72. https://doi.org/10.1016/j.sbi.2007.03.014 PMID: 17395455

28. Boras BW, Hirakis SP, Votapka LW, Malmstrom RD, Amaro RE, & McCulloch AD. (2015). Bridging scales through multiscale modeling: A case study on protein kinase A. *Frontiers in Physiology*, 6(SEP), 250. https://doi.org/10.3389/fphys.2015.00250 PMID: 26441670

29. Kitano H. (2002). Computational systems biology. *Nature*, 420(November), 206–210. https://doi.org/10.1038/nature01254 PMID: 12432404

30. Tesmer JJG and Sprang SR. (1998). The structure, catalytic mechanism and regulation of adenylyl cyclase. *Current opinion in structural biology*, 8(6), 713–719. https://doi.org/10.1016/S0959-440X(98)80090-0 PMID: 9914249

31. Steitz TA. (1993). DNA-and RNA-dependent DNA polymerases. *Current Opinion in Structural Biology*, 3(1), 31–38. https://doi.org/10.1016/0959-440X(93)90198-T

32. Nakamura T, Zhao Y, Yamagata Y, Hua YJ, and Yang W. (2012). Watching DNA polymerase η make a phosphodiester bond. *Nature*, 487(7406), 196–201. https://doi.org/10.1038/nature11181 PMID: 22785315

33. Zhang YF, and Cragg SJ. (2017) Pauses in Striatal Cholinergic Interneurons: What is Revealed by Their Common Themes and Variations? *Frontiers in Systems Neuroscience* 11:80. https://doi.org/10.3389/fnsys.2017.00080 PMID: 29163075

34. Nair AG. (2018). Modeling Biochemical Network Involved in Striatal Dopamine Signaling (TRITA-EECS-AVL; 2018:7). *KTH Royal Institute of Technology*.

35. Cooper DF. (2003) Regulation and organization of adenylyl cyclases and cAMP, *Biochem. J.* 375, 517–529. https://doi.org/10.1042/BJ20031061 PMID: 12940771

36. Cooper DF, and Crossthwaite AJ. (2006) Higher-order organization and regulation of adenylyl cyclases, *Trends in Pharmacological Sciences*, 27(8): 426–431. https://doi.org/10.1016/j.tips.2006.06.002 PMID: 16820220

37. Xie K, Masuho I, Shih C-C, Cao Y, Sasaki K, Lai CWJ, Han P-L, Ueda H, Dessauer CW, Ehrlich ME, Xu B, Willardson BM, Martemyanov KA. (2015) Stable G protein-effector complexes in striatal neurons: mechanism of assembly and role in neurotransmitter signaling, *eLife* 4: e10451. https://doi.org/10.7554/eLife.10451 PMID: 26613416

38. Hahn DK, Tusell JR, Sprang SR & and Chu X. (2015) Catalytic Mechanism of Mammalian Adenylyl Cyclase: A Computational Investigation, *Biochemistry*, 54(40), 6252–6262. https://doi.org/10.1021/acs.biochem.5b00655 PMID: 26393535

39. Navarro G, Cordomí A, Casadó-Anguera, Moreno E, Cai N-S, Cortés A, Canela EI, Dessauer CW, Casadó V, Pardo L, Lluís C, and Ferré S. Evidence for functional pre-coupled complexes of receptor heteromers and adenylyl cyclase, *Nature Communications* 9, Article number: 1242 (2018),https://doi.org/10.1038/s41467-018-03522-3

40. Iwamoto T, Iwatsubo K, Okumura S, Hashimoto Y, Tsunematsu T, Toya Y, Hervé D, Umemura S and Ishikawa Y (2004), Disruption of type 5 adenylyl cyclase negates the developmental increase in Gαolf expression in the striatum, *FEBS Letters*, 564, https://doi.org/10.1016/S0014-5793(04)00333-3

41. Xie K, Masuho I, Brand C, Dessauer CW, Martemyanov KA (2012) The complex of G protein regulator RGS9-2/Gβ5 controls sensitization and signaling kinetics of type 5 adenylyl cyclase. *Sci Signal* 5:ra63, https://doi.org/10.1126/scisignal.2002922 PMID: 22932702.

42. Taussig R, Tang W-J, Hepler JR, and Gilman AG. (1994) Distinct Patterns of Bidirectional Regulation of Mammalian Adenylyl Cyclases, *The Journal of Biological Chemistry*, Vol. 269, No. 8, pp. 6093 –6100 PMID: 8119955

43. Fino E, Glowinski J, & Venance L. (2005) Bidirectional Activity-Dependent Plasticity at Corticostriatal Synapses, *The Journal of Neuroscience* 25(49): 11279–11287 https://doi.org/10.1523/JNEUROSCI.4476-05.2005 PMID: 16339023

44. Pawlak V and Kerr JND. (2008) Dopamine Receptor Activation is Required for Corticostriatal Spike-Timing-Dependent Plasticity, *The Journal of Neuroscience* 28(10): 2435–2446 https://doi.org/10.1523/JNEUROSCI.4402-07.2008 PMID: 18322089

45. Shen W, Flajolet M, Greengard P, and Surmeier J. (2008) Dichotomous Dopaminergic control of striatal synaptic plasticity, *Science* 321(5890): 848–851 https://doi.org/10.1126/science.1160575 PMID: 18687967

46. Fisher SD, Robertson PB, Black MJ, Redgrave P, Sagar MA, Abraham WC, and Reynolds JNJ (2017), Reinforcement determines the timing dependence of corticostriatal synaptic plasticity in vivo, *Nature Communications*, 8:334, https://doi.org/10.1038/s41467-017-00394-x PMID: 28839128

47. Lui Y-H, Wenzel-Seifert K, & Seifert R. (2001). The olfactory G protein Gαolf possesses a lower GDP-affinity and deactivates more rapidly than Gsαshort: Consequences for receptor-coupling and adenylyl cyclase activation. *Journal of Neurochemistry*, 78(2), 325–338. https://doi.org/10.1046/j.1471-4159.2001.00422.x PMID: 11461968

48. Tong R, Wade RC, & Bruce NJ. (2016). Comparative electrostatic analysis of adenylyl cyclase for isoform dependent regulation properties. *Proteins: Structure, Function and Bioinformatics*, 84(13), 1844–1858. https://doi.org/10.1002/prot.25167 PMID: 27667304

49. Taussig R, Iniguez-Lluhi JA, & Gilman AG. (1992). Inhibition of Adenylyl Cyclase by Giα. *Science*, 261, 218–221.

50. Dessauer C. (2009) Adenylyl Cyclase–A-kinase Anchoring Protein Complexes: The Next Dimension in cAMP Signaling. *Molecular Pharmacology* 76 (5): 935–941 https://doi.org/10.1124/mol.109.059345 PMID: 19684092

51. Brand C. S., Sadana R., Malik M., Smrcka A. V., & Dessauer C. W. (2015), Adenylyl Cyclase 5 Regulation by Gβγ Involves Isoform-Specific Use of Multiple Interaction Sites, *Molecular Pharmacology*, 88, 758–767. https://doi.org/10.1124/mol.115.099556 PMID: 26206488

52. Hersch SM, Gutekunst CA, Rees HD, Heilman CJ and Levey AI. Distribution of m1-m4 muscarinic receptor proteins in the rat striatum: light and electron microscopic immunocytochemistry using subtype- specific antibodies. *Journal of Neuroscience* 1994; 14 (5) 3351–3363; https://doi.org/10.1523/JNEUROSCI.14-05-03351.1994

53. Hersch SM, Ciliax BJ, Gutekunst CA, Rees HD, Heilman CJ, Yung KK, Bolam JP, Ince E, Yi H and Levey AI, Electron microscopic analysis of D1 and D2 dopamine receptor proteins in the dorsal striatum and their synaptic relationships with motor corticostriatal afferents. *Journal of Neuroscience* 1995; 15 (7) 5222–5237; https://doi.org/10.1523/JNEUROSCI.15-07-05222.1995

54. Seebacher T, Linder JU, & Schultz JE. (2001). An isoform-specific interaction of the membrane anchors affects mammalian adenylyl cyclase type V activity, *European Journal of Biochemistry*, 268, 105–110. https://doi.org/10.1046/j.1432-1327.2001.01850.x PMID: 11121109

55. Whisnant RE, Gilman AG, & Dessauer CW. (1996) Interaction of the two cytosolic domains of mammalian adenylyl cyclase. *Proceedings of the National Academy of Sciences of the United States of America* 93(13): p. 6621–6625. https://doi.org/10.1073/pnas.93.13.6621 PMID: 8692867

56. Van Keulen SC, & Rothlisberger U. (2017a). Effect of N-Terminal Myristoylation on the Active Conformation of Gαi1-*GTP. Biochemistry*, 56(1), 271–280. https://doi.org/10.1021/acs.biochem.6b00388 PMID: 27936598

57. Qi C, Sorrentino S, Medalia O, and Korkhov VM. (2019) The structure of a membrane adenylyl cyclase bound to an activated stimulatory G protein. *Science* 364(6438): 389–394. https://doi.org/10.1126/science.aav0778 PMID: 31023924

58. Eswar N, Webb B, Marti-Renom MA, Madhusudhan MS, Eramian D, Shen M, Pieper U, & Sali A. (2006). Comparative protein structure modeling using modeller. *Current Protocols in Bioinformatics*, 5–6.

59. Martí-Renom MA, Stuart AC, Fiser A, Sánchez R, Melo F & Sali A. (2000). Comparative protein structure modeling of genes and genomes. *Annual Review of Biophysics and Biomolecular Structure*, 29 (1):291–325.

60. De Vries SJ, van Dijk M, & Bonvin AM. J. J. (2010). The haddock web server for data-driven biomolecular docking. *Nature Protocols*, 5(5):883–897, 4. https://doi.org/10.1038/nprot.2010.32 PMID: 20431534

61. Bekker H, Berendsen HJC, Dijkstra EJ, Achterop S, Van Drunen R, Van der Spoel D, Sijbers A, Keegstra H, and Renardus MKR. (1993). Gromacs: A parallel computer for molecular dynamics simulations. *Physics Computing*, 92:252–256.

62. Abraham MJ, Murtola T, Schulz R, Páll S, Smith JC, Hess B, Lindahl E. (2015). GROMACS: High performance molecular simulations through multi-level parallelism from laptops to supercomputers. *SoftwareX* 1, 19–25.

63. Hornak V, Abel R, Okur A, Strockbine B, Roitberg A & Simmerling C. (2006). Comparison of multiple Amber force fields and development of improved protein backbone parameters. Proteins: Structure, Function, and *Bioinformatics*. 65(3), 712–725.

64. Jorgensen WL, Chandrasekhar J, Madura JD, Impey RW & Klein ML. (1983). Comparison of simple potential functions for simulating liquid water. *The Journal of Chemical Physics*. 79(2), 926–935.

65. Meagher KL, Redman LT, & Carlson HA. (2003). Development of polyphosphate parameters for use with the AMBER force field. *Journal of Computational Chemistry*, 24(9), 1016–1025. https://doi.org/10.1002/jcc.10262 PMID: 12759902

66. Joung IS & Cheatham TE III. (2008). Determination of alkali and halide monovalent ion parameters for use in explicitly solvated biomolecular simulations. *The Journal of Physical Chemistry B*. 112(30), 9020–9041. https://doi.org/10.1021/jp8001614 PMID: 18593145

67. Allnér O, Nilsson L, & Villa A. (2012). Magnesium ion–water coordination and exchange in biomolecular simulations. *Journal of Chemical Theory and Computation*., 8(4), 1493–1502. https://doi.org/10.1021/ct3000734 PMID: 26596759

68. Hess BP. (2008). LINCS: A parallel linear constraint solver for molecular simulation. *Journal of Chemical Theory and Computation*. 4(1), 116–122. 7 https://doi.org/10.1021/ct700200b PMID: 26619985

69. Martinez M, Bruce NJ, Romanowska J, Kokh DB, Ozboyaci M, Yu X, Öztürk MA, Richter S, & Wade RC. (2015). SDA 7: A modular and parallel implementation of the simulation of diffusional association software. *Journal of Computational Chemistry*, 36(21), 1631–1645. https://doi.org/10.1002/jcc.23971 PMID: 26123630

70. Gabdoulline RR & Wade RC. (1996). Effective Charges for Macromolecules in Solvent. *Journal of Physical Chemistry*, 100(9), 3868–3878. https://doi.org/10.1021/jp953109f

71. Elcock AH, Gabdoulline RR, Wade RC, & McCammon JA. (1999). Computer simulation of protein-protein association kinetics: acetylcholinesterase-fasciculin. *Journal of Molecular Biology*, 291(1), 149–162. https://doi.org/10.1006/jmbi.1999.2919 PMID: 10438612

72. Gabdoulline RR & Wade RC. (2001).Protein-protein association: investigation of factors influencing association rates by brownian dynamics simulations. *Journal of Molecular Biology*, 306(5), 1139–1155. https://doi.org/10.1006/jmbi.2000.4404 PMID: 11237623

73. Baker NA, Sept D, Joseph S, Holst MJ, & McCammon JA. (2001). Electrostatics of nanosystems: application to microtubules and the ribosome. *Proceedings of the National Academy of Sciences U. S. A.*, 98(18), 10037–10041. https://doi.org/10.1073/pnas.181342398 PMID: 11517324

74. Bondi A. (1964). van der Waals Volumes and Radii. *The Journal of Physical Chemistry*, 68(3), 441–451. https://doi.org/10.1021/j100785a001

75. Bruccoleri R, Novotny J, Davis M, & Sharp K. (1997). Finite difference Poisson-Boltzmann electrostatic calculations: Increased accuracy achieved by harmonic dielectric smoothing and charge antialiasing. *Journal of Computational Chemistry*, 18(2), 268–276. https://doi.org/10.1002/(SICI)1096-987X(19970130)18:2<268::AID-JCC11>3.0.CO;2-E

76. Northrup SH, Allison SA, & McCammon JA. (1984). Brownian dynamics simulation of diffusion-influenced bimolecular reactions. *The Journal of Chemical Physics*, 80(4), 1517. https://doi.org/10.1063/1.446900

77. García De La Torre J, Huertas ML, & Carrasco B. (2000). Calculation of hydrodynamic properties of globular proteins from their atomic-level structure. *Biophysical Journal*, 78(2), 719–730. https://doi.org/10.1016/S0006-3495(00)76630-6 PMID: 10653785

78. Ortega A, Amorós D, & García de la Torre J. (2011). Prediction of hydrodynamic and other solution properties of rigid proteins from atomic- and residue-level models. *Biophysical Journal*, 101(4), 892–898. https://doi.org/10.1016/j.bpj.2011.06.046 PMID: 21843480

79. Scholich K, Mullenix JB, Wittpoth C, Poppleton HM, Pierre SC, Lindorfer MA, Garrison JC, Patel TB. (1999) Facilitation of signal onset and termination by adenylyl cyclase. *Science* 283:1328–1331, https://doi.org/10.1126/science.283.5406.1328 PMID: 10037603